iScience

CellPress
OPEN ACCESS

Article

Identification and differential usage of a host metalloproteinase entry pathway by SARS-CoV-2 Delta and Omicron

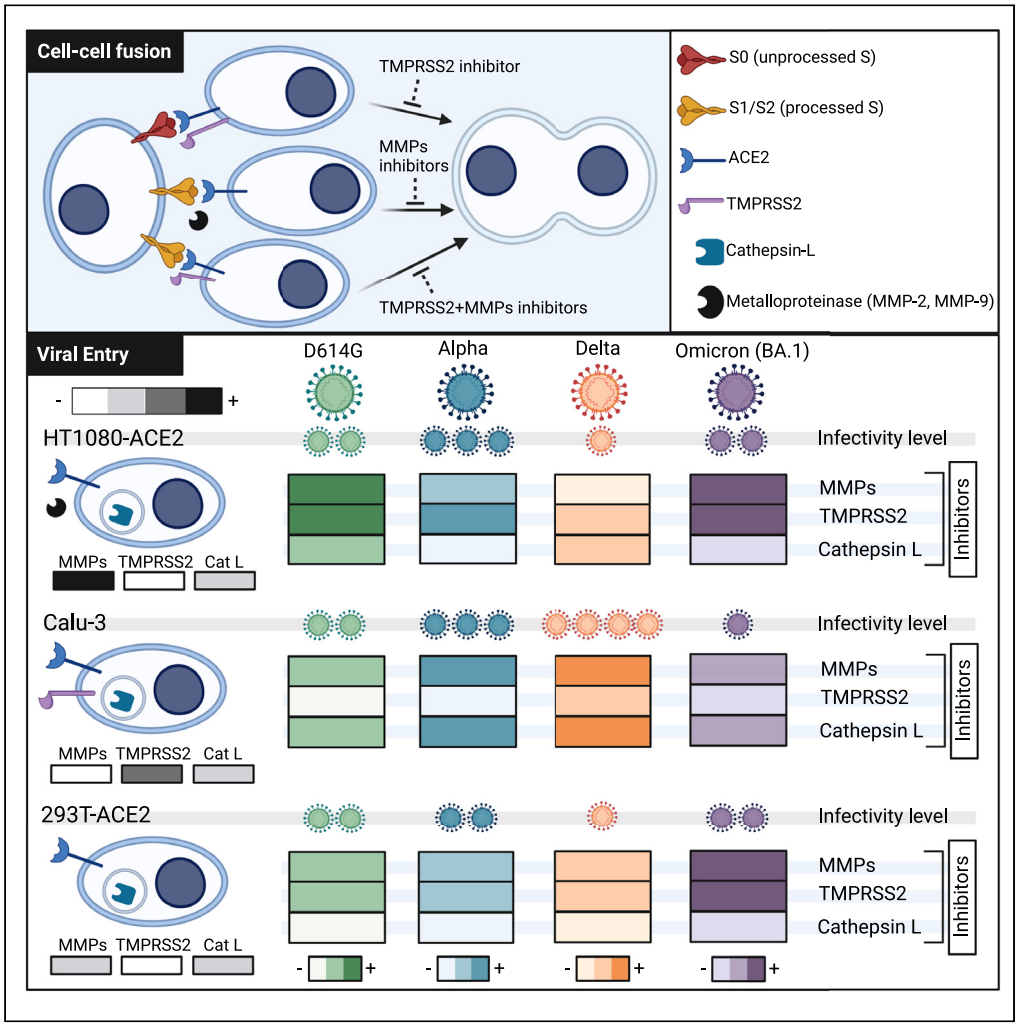

Mehdi Benlarbi, Geneviève Laroche, Corby Fink, ..., Gregory A. Dekaban, Jimmy D. Dikeakos, Marceline Côté

marceline.cote@uottawa.ca

Highlights

MMP-2 and MMP-9 enable SARS-CoV-2 S-mediated syncytia in the absence of TMPRSS2

SARS-CoV-2 can enter cells via MMPs in a TMPRSS2- and cathepsin-independent manner

MMP-dependent S activation requires prior S1/S2 processing

Delta S can readily use MMPs for entry while Omicron S cannot

Benlarbi et al., iScience 25, 105316
November 18, 2022
https://doi.org/10.1016/j.isci.2022.105316

iScience

CellPress
OPEN ACCESS

Article

Identification and differential usage of a host metalloproteinase entry pathway by SARS-CoV-2 Delta and Omicron

Mehdi Benlarbi,[1,2,3,13] Geneviève Laroche,[1,2,3,13] Corby Fink,[4,5] Kathy Fu,[1,2,3] Rory P. Mulloy,[1,2,3] Alexandra Phan,[1,2,3] Ardeshir Ariana,[1,2,3] Corina M. Stewart,[1,2,3] Jérémie Prévost,[6,7] Guillaume Beaudoin-Bussières,[6,7] Redaet Daniel,[1,2,3] Yuxia Bo,[1,2,3] Omar El Ferri,[1,2,3] Julien Yockell-Lelièvre,[1,2,8,9] William L. Stanford,[1,2,8,9] Patrick M. Giguère,[1] Samira Mubareka,[10,11] Andrés Finzi,[6,7] Gregory A. Dekaban,[4,5] Jimmy D. Dikeakos,[4,5] and Marceline Côté[1,2,3,12,*]

SUMMARY

The severe acute respiratory syndrome coronavirus-2 (SARS-CoV-2) spike glycoprotein (S) binds to angiotensin-converting enzyme 2 (ACE2) to mediate membrane fusion via two distinct pathways: 1) a surface, serine protease-dependent or 2) an endosomal, cysteine protease-dependent pathway. In this study, we found that SARS-CoV-2 S has a wider protease usage and can also be activated by TMPRSS13 and matrix metalloproteinases (MMPs). We found that MMP-2 and MMP-9 played roles in SARS-CoV-2 S cell-cell fusion and TMPRSS2- and cathepsin-independent viral entry in cells expressing high MMP levels. MMP-dependent viral entry required cleavage at the S1/S2 junction in viral producer cells, and differential processing of variants of concern S dictated its usage; the efficiently processed Delta S preferred metalloproteinase-dependent entry when available, and less processed Omicron S was unable to us metalloproteinases for entry. As MMP-2/9 are released during inflammation, they may play roles in S-mediated cytopathic effects, tropism, and disease outcome.

INTRODUCTION

Coronavirus disease-2019 (COVID-19) is caused by severe acute respiratory syndrome coronavirus-2 (SARS-CoV-2), a highly transmissible positive sense single-stranded RNA virus. The clinical presentation of COVID-19 ranges from asymptomatic or mild to severe disease, including pneumonitis and acute respiratory distress syndrome (Huang et al., 2020). Severe COVID-19 is characterized by an uncontrolled release of cytokines, leading to hyperinflammation, tissue damage, and dysregulated immune responses. The persistence of these responses often results in multi-organ damage and failure (Tay et al., 2020). In addition, upon SARS-CoV-2 infection, pneumocyte syncytia formation is more prevalent in COVID-19 patients with severe chronic respiratory diseases, suggesting a potential hallmark of disease pathogenesis (Braga et al., 2021).

Membrane fusion is mediated by viral fusion proteins that protrude from the viral membrane or are exposed at the cell surface of infected cells. It can occur during viral entry or between adjacent cells expressing viral fusion proteins and/or its receptor, causing syncytium formation. To catalyze the merging of membranes during viral entry and cell-to-cell fusion, viral fusion proteins undergo extensive conformational changes, from a high-energy metastable state to a highly stable low-energy state (Harrison, 2015). This conformational rearrangement is induced by virus-specific triggers such as receptor binding, low pH, and/or proteolytic cleavage (Harrison, 2015). For SARS-CoV-2, the viral fusion protein is the spike glycoprotein (S). S is composed of two subunits: S1, which mediates attachment to the host cell receptor angiotensin-converting enzyme 2 (ACE2) and, S2, which facilitates membrane fusion (Shang et al., 2020; Wan et al., 2020; Letko et al., 2020). SARS-CoV-2 and SARS-CoV-1 are related pathogenic betacoronaviruses that share a common host receptor (Li et al., 2003), ACE2, and both require a two-step sequential cellular protease cleavage of the S protein at the S1/S2 junction and at an S2′ site for entry (Figure 1A) (Hoffmann et al., 2020b; Jackson et al., 2022). Cleavage of the S1/S2 junction reveals the S2′ site, which is further processed to expose the fusion peptide allowing membrane fusion (Belouzard et al., 2009) (Figure 1A).

[1]Department of Biochemistry, Microbiology and Immunology, University of Ottawa, Ottawa, ON K1H 8M5, Canada

[2]Ottawa Institute of Systems Biology, University of Ottawa, Ottawa, ON K1H 8M5, Canada

[3]Centre for Infection, Immunity and Inflammation, University of Ottawa, Ottawa, ON K1H 8M5, Canada

[4]Department of Microbiology & Immunology, Schulich School of Medicine & Dentistry Western University, London, ON N6A 5C1, Canada

[5]Molecular Medicine Research Laboratories, Robarts Research Institute, University of Western Ontario, London, ON N6A 5C1, Canada

[6]Centre de Recherche du CHUM, Montréal, QC H2X 0A9, Canada

[7]Département de Microbiologie, Infectiologie et Immunologie, Université de Montréal, Montréal, QC H3C 3J7, Canada

[8]The Ottawa Hospital Research Institute, Ottawa, ON K1H 8L6, Canada

[9]Department of Cellular and Molecular Medicine, University of Ottawa, Ottawa, ON K1H 8M5, Canada

[10]Sunnybrook Research Institute, Toronto, ON M4N 3M5, Canada

[11]Department of Laboratory Medicine and Pathobiology, University of Toronto, Toronto, ON M5S 1A8, Canada

[12]Lead contact

Continued

However, unlike that of SARS-CoV-1, SARS-CoV-2 S possesses an arginine-rich motif within the S1/S2 cleavage site enabling recognition and cleavage at the S1/S2 boundary by furin or furin-like enzymes in the virus-producer cell (Tang et al., 2021). The furin cleavage site has been shown to be critical for SARS-CoV-2 infection in human lung cells and transmissibility in ferrets (Peacock et al., 2021a; Hoffmann et al., 2020a). Moreover, variants of concern such as Alpha, Delta, and more recently Omicron possess mutations within the S1/S2 furin cleavage site that affect furin cleavage efficiency and S fusogenic activity (Lubinski et al., 2022; Meng et al., 2022; Saito et al., 2021).

Previous studies have defined two possible routes of entry used by SARS-CoV-2 and SARS-CoV-1: an early cell surface pathway following activation by surface serine proteases, notably the transmembrane serine protease 2 (TMPRSS2), and a late-endocytic pathway using endolysosomal cathepsins (Murgolo et al., 2021). Host cell protease expression dictates which viral entry pathways are preferred and could explain why some drugs targeting one but not both pathways are not effective at reducing the SARS-CoV-2 burden in patients (Horby et al., 2020). S glycoproteins expressed at the surface of infected cells also require similar triggers to induce syncytia formation (Buchrieser et al., 2020). Interestingly, previous studies have reported SARS-CoV-2 S-mediated cell-cell fusion in the absence of TMPRSS2 expression (Nguyen et al., 2020; Hörnich et al., 2021); however, the identification of the activating protease(s) or if this mechanism represents an additional cell entry pathway remain unknown.

Here we show that in the absence of TMPRSS2, SARS-CoV-2 S can use the matrix metalloproteinases (MMPs), MMP-2 and 9, to induce cell-cell fusion. In cells expressing high levels of MMP-2/9 such as HT1080 cells, infection and syncytia formation induced by native SARS-CoV-2 Alpha were significantly reduced by MMP inhibitors. We also investigated MMP roles in a viral entry using lentiviral pseudotypes and virus-like particles harboring S of wild-type D614G or variants of concern and found that the various S glycoproteins differentially used the MMP pathway and preferential usage correlated with the extent of S1/S2 processing and syncytia formation. Previous studies have reported increased serum levels of MMPs such as MMP-9 in patients with severe COVID-19 (Gelzo et al., 2022). Therefore, our studies suggest that in the context of hyperinflammation and dysregulated immune responses, MMPs could play a role in facilitating SARS-CoV-2 viral entry and syncytia formation, expanding tropism to TMPRSS2 negative cells, and exacerbating COVID-19.

RESULTS

Cell-cell fusion mediated by SARS-CoV-2 S can occur in a surface serine protease-independent manner but remains angiotensin-converting enzyme-dependent and is enhanced by TMPRSS2 and TMPRSS13

To study the host factors required for the SARS CoV-2 S activation and compare them to host factors required for SARS-CoV-1 S, we first sought to establish a syncytium-formation assay. Parental 293T cells or 293T cells engineered to overexpress human ACE2 were transfected with plasmids encoding S and green fluorescent protein (GFP) to visualize large areas of fused cells that can be distinguishable from single cells. A plasmid encoding for the serine protease, TMPRSS2, or an empty vector, pCAGGS, was also transfected to assess S dependency on surface serine protease fusion activity. As expected, we found that SARS-CoV-1 S can only induce syncytia formation in the presence of both ACE2 and TMPRSS2 (Figure 1B) (Hoffmann et al., 2020b; Glowacka et al., 2011). In addition, the ACE2/TMPRSS2-dependent SARS-CoV-1 S cell fusion was abrogated when cells were treated with Camostat, a serine protease inhibitor, further indicating that cell fusion by SARS-CoV-1 S requires serine protease activity (Figure 1B). In contrast, SARS CoV-2 S-mediated syncytia were observed even in the absence of TMPRSS2, yet their formation was still dependent on ACE2 expression (Figure 1B). Interestingly, the incubation of cells with Camostat did not reduce syncytia formation by SARS CoV-2 S, in the presence or absence of TMPRSS2 (Figure 1B). These results suggest that, unlike SARS-CoV-1 S, SARS CoV-2 S-mediated fusion can occur independently of surface serine protease activity.

ACE2 dependence and the contribution of TMPRSS2 were further assessed by incubating SARS-CoV-2 S-expressing 293T cells with soluble ACE2. In these conditions, an ACE2 dose-dependent increase in S-mediated fusion and a robust enhancement of cell-cell fusion when TMPRSS2 was co-expressed was observed (Figure S1). To further quantify cell-cell fusion, we used a bimolecular fluorescence complementation assay based on the separate expression of fragments of the yellow fluorescent protein, Venus, fused to a leucine zipper in effector and target cell populations (ZIP Venus assay) (Figure 1C) (Carter-Timofte

[13]These authors contributed equally

*Correspondence: marceline.cote@uottawa.ca

https://doi.org/10.1016/j.isci.2022.105316

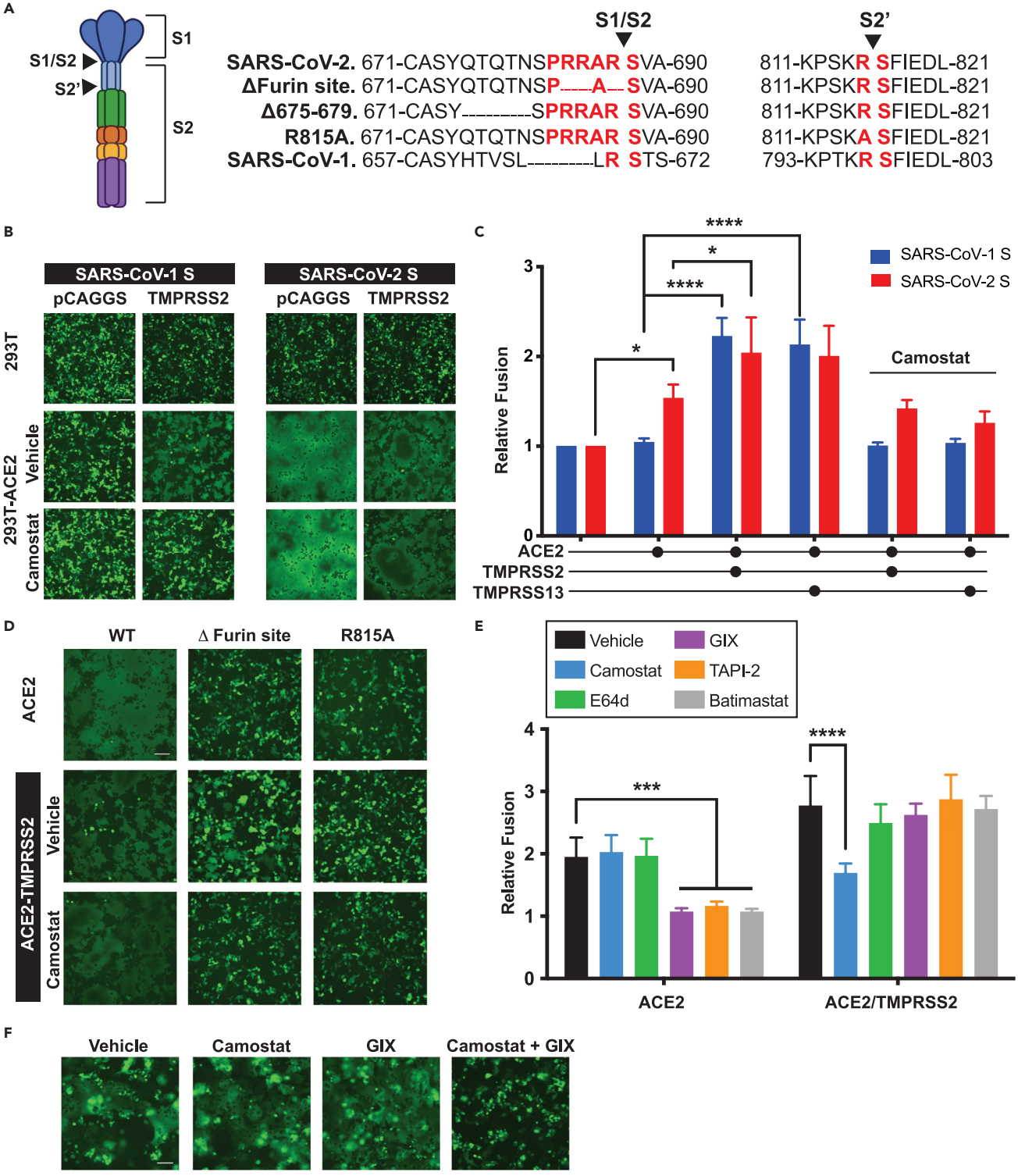

Figure 1. SARS-CoV-2 S can mediate cell-cell fusion in a metalloproteinase-dependent manner

(A) Schematics of the S glycoprotein and amino acid sequences at the S1/S2 and S2′ cleavage sites of mutants used in this study. In green: fusion peptide, in orange and yellow: N- and O- heptad repeats respectively, in purple: transmembrane domain, in red: amino acids surrounding the cleavage sites. Arrow heads depict the cleavage site.

Figure 1. *Continued*

(B and D) (Created with BioRender) (B, D) 293T or 293T stably expressing ACE2 (293T-ACE2) were co-transfected with plasmids encoding GFP, SARS-CoV-1 or SARS-CoV-2 S WT or indicated mutants, and TMPRSS2, or with an empty vector, in the presence or absence of Camostat (25 μM). Syncytia formation was visualized 24 h post-transfection using fluorescence microscopy.

(C and E) Effector 293T cells transfected with plasmids encoding SARS-CoV-1 or SARS-CoV-2 S and ZipVenus1, were co-cultured with target 293T cells transfected with plasmid encoding ZipVenus 2, ACE2 and TMPRSS2, TMPRRS13 or empty vector, in the presence or absence of indicated protease inhibitors (Camostat 25 μM, E64days 10 μM, GIX 25402X3 (GIX) 10 μM, TAPI-2 40 μM, Batimastat 10 μM). Fluorescence generated by the reconstitution of ZIPVenus upon cell-cell fusion was measured after 4 h of co-culture.

(F) 293T cells transfected with plasmids encoding GFP and SARS-CoV-2 S were co-cultured (1:1 ratio) with Calu-3 cells in the presence of the indicated inhibitors (Camostat 25 μM, GIX 10 μM). Syncytia were visualized 24 h post-transfection using fluorescence microscopy. Pictures are representative images of at least 3 independent experiments ($n \leq 3$). Each bar graph shows the mean of triplicate values of 3 independent experiments with error bars showing SD. Significance was determined by ANOVA (one-way ANOVA) followed by a Dunnett's multiple comparisons test. p-value lower than 0.05 was used to indicate a statistically significant difference (****, $p < 0.0001$, ***, $p < 0.001$, **, $p < 0.01$, *, $p < 0.05$). The scale bar represents 300 μm.

See also Figure S1.

et al., 2021). This assay allows for the quantitative measurement of the extent of cell-cell fusion using fluorescence. Previous studies on SARS-CoV-1 S and recent studies on SARS CoV-2 S revealed that other surface serine proteases can also activate these viral fusion proteins (Zang et al., 2020; Kishimoto et al., 2021; Hoffmann et al., 2021; Bertram et al., 2011; Zhang et al., 2020). Here we sought to validate a role for TMPRSS13 in our assay given its broad expression in the respiratory tract and by immune cells, in addition to its previously reported implications in infection (Laporte et al., 2021). Target cells transfected with various combinations of plasmids encoding ACE2 and ones encoding TMPRSS2 or TMPRSS13 were co-cultured with effector cells encoding S from SARS-CoV-1 or SARS CoV-2. We found that expression of TMPRSS2 or TMPRSS13 enhanced SARS-CoV-1 and SARS-CoV-2 S mediated cell-cell fusion in an ACE2-dependent manner and that the contribution of TMPRSS2/13 in cell-cell fusion was sensitive to Camostat treatment (Figure 1C). Like the results of the syncytia formation assay, cell-cell fusion was observed in a TMPRSS2/13-independent manner for SARS-CoV-2 S but not SARS-CoV-1 (Figure 1C). These results agree with previous studies and indicate that the fusion activity of SARS CoV-1 and SARS-CoV-2 S can be activated by several surface serine proteases, yet only SARS-CoV-2 can induce cell-cell fusion in the absence of those proteases.

SARS-CoV-2 S2′ site is processed by both serine proteases and metalloproteinases, and cell-cell fusion is abrogated by metalloproteinase inhibitors

Previous studies on coronavirus S glycoproteins showed that the activation of the fusion activity of S required sequential proteolytic cleavage at the S1/S2 boundary and at an S2′ site, both of which can be performed by several different surface serine proteases or endosomal cathepsin proteases during viral entry (Belouzard et al., 2009; Le Coupanec et al., 2021). To confirm that these protease cleavage steps are also required for the TMPRSS2-independent fusion observed with SARS-CoV-2 S, we next tested the fusion activity of S constructs mutated at the S1/S2 junction (Δ furin site) and the S2′ site (R815A) (Figure 1A). We found that SARS-CoV-2 S-mediated syncytia formation still occurred when the furin cleavage site was removed, but only in the presence of TMPRSS2 (Figure 1D). In addition, and similar to reports from other studies, a mutation at the S2′ site inactivated the fusion activity of S, which could not be rescued by TMPRSS2 expression (Figure 1D) (Yu et al., 2022; Hörnich et al., 2021). These results indicate that the S2′ site of SARS CoV-2 S is critical for fusion activation and that the TMPRSS2-independent fusion requires processing at the S1/S2 boundary.

The requirement for an intact S2′ site also suggested that the cell-cell fusion in the absence of TMPRSS2 or TMPRSS13 required proteolysis by an unknown protease expressed at the surface or secreted by these cells that are not inhibited by Camostat. Likely candidates include members of the broad family of metalloproteases which are active at neutral pH and can be membrane-bound or secreted from a variety of cells. To identify the unknown protease(s) responsible for the fusion, we used the cell-cell fusion assay and incubated the cells with inhibitors of serine proteases (Camostat), late endosome/lysosomal cysteine proteases (E64days), and metalloproteinases (GI 254023X (GIX), TAPI-2, and batimastat). As expected, Camostat and E64days did not affect SARS-CoV-2 S-mediated cell-cell fusion in the absence of TMPRSS2. However, all the metalloproteinase inhibitors completely blocked fusion (Figure 1E) suggesting that one or multiple metalloproteinases expressed by 293T-ACE2 cells can trigger SARS-CoV-2 S fusion activity. In addition, these metalloproteinase inhibitors were rendered ineffective when TMPRSS2 was expressed (Figure 1E), suggesting that TMPRSS2 could compensate for the inhibition of metalloproteinase activity. However, metalloproteinase-dependent fusion was still observed in 293T-TMPRSS2/ACE2 cells treated with Camostat

(Figures 1D and 1E). To explore this further, we co-cultured 293T cells expressing SARS-CoV-2 S and GFP with Calu-3 cells which endogenously express ACE2 and surface serine proteases such as TMPRSS2 (Saccon et al., 2021). We found that SARS-CoV-2 S efficiently promoted cell-cell fusion which was insensitive to the action of single inhibitors and could only be blocked when a combination of serine protease and metalloproteinase inhibitors were used (Figure 1F). These results indicate that serine proteases and metalloproteinases perform a redundant cleavage step, presumably at the S2′ site.

SARS-CoV-2 S can mediate cell entry via a metalloproteinase-dependent pathway

Previous studies had also reported SARS-CoV-2 S batimastat-sensitive cell-cell fusion, yet this broad metalloproteinase inhibitor had no effect on viral entry in the cell lines tested (Nguyen et al., 2020; Hörnich et al., 2021). However, since these and our results show that metalloproteinases can activate S for cell-cell fusion, the expectation is that these proteases should also be able to mediate viral entry. To investigate this, we tested viral entry in 293T-ACE2 and Calu-3 cells using lentiviral pseudotypes. Like other studies (Koch et al., 2021), we found that SARS-CoV-2 and SARS-CoV-1 S-mediated entry was strongly inhibited by E64days in 293T-ACE2 cells, and by Camostat in Calu-3 cells (Figures 2A and 2B). In addition, a slight reduction in the entry of SARS-CoV-2 pseudotypes in 293T-ACE2 cells was observed in the presence of metalloproteinase inhibitors (Figure 2A). However, the dramatic decrease in entry after treatment within E64days indicated that the cathepsin entry pathway is the preferred route in these cells.

We surmised that while expression of metalloproteinases in 293T-ACE2 cells might be sufficient to induce cell-cell fusion, the levels could be too low to mediate effectively viral entry. We, therefore, measured metalloproteinase mRNA levels in 293T cells and various cell lines using quantitative reverse transcription PCR (RT-qPCR) (Figure 2C). We found that HT1080 cells express high mRNA levels of MMP-2 and MMP-9, which are targets of GIX and TAPI-2 (Figure 2C) (Zocchi et al., 2016; Raissi et al., 2014). The secretion and elevated activity of MMP-2 and MMP-9 produced by these cells were also confirmed by *in gel* gelatin zymography which allows the visualization of electrophoretically resolved MMP-2 and MMP-9 via the degradation of their gelatin substrate leaving white bands when the gelatin polyacrylamide gel is stained with Coomassie Blue (Figure 2D). We also found that unlike the Calu-3 cells, the HT1080-ACE2 cells do not express TMPRSS2 as measured by cell surface staining and flow cytometry (Figure S2), indicating that these cells would allow for the testing of a potential role of matrix metalloproteinases in SARS-CoV-2 entry. HT1080 cells were transfected with a plasmid encoding ACE2 and infected with SARS-CoV-2 lentiviral pseudotypes. Strikingly, in these cells, SARS-CoV-2 S-mediated entry was insensitive to E64days and Camostat, but completely abrogated by TAPI-2 and GIX. In comparison, entry of pseudotypes bearing SARS-CoV-1 S was blocked by E64days and those with VSV-G remained mostly unaffected, although a slight inhibition by Camostat was noted (Figure 2E). These results indicate that in cells expressing high levels of secreted MMPs, SARS-CoV-2 S entry was mediated via a previously unrecognized entry route that is cysteine/serine protease-independent and metalloproteinase-dependent.

A viral-like-particle system reveals distinct S processing efficiencies and differential usage of the metalloproteinase-dependent entry pathway among SARS-CoV-2 variants

Although lentiviral pseudotypes are suitable, well-established surrogate systems to investigate viral entry, differential budding sites between lentiviruses and coronaviruses can lead to variations in S glycoprotein processing (Fu et al., 2021; Wang et al., 2021b). Since our cell-cell fusion assays clearly demonstrated that the processing of S at the S1/S2 junction is required for metalloproteinase-dependent activation of S (Figure 1D), we sought to validate our results using virus-like particles (VLPs). As described previously, SARS-CoV-2 VLPs are produced in cells after co-expression of the four SARS-CoV-2 structural proteins (S, M, E, N) and a reporter gene, thus more accurately recapitulating SARS-CoV-2 egress and entry compared to lentiviral pseudotypes (Syed et al., 2021a). We found that lentiviruses incorporate mostly fully processed S (Figure 3A), while S on the VLPs were a mixture of unprocessed (S0) and cleaved S (Figure 3B), which agrees with previous studies (Zhang et al., 2022; Ou et al., 2020; Zeng et al., 2020; Plescia et al., 2021; Syed et al., 2021a). Interestingly, highly transmissible variants of concern Alpha and Delta, which both have mutations at P681 near the S1/S2 furin cleavage site (Lubinski et al., 2022; Peacock et al., 2021b), display differential S processing when expressed at the surface of VLPs. Specifically, the Delta variant S, which harbors a P681R mutation, is processed more efficiently than both the alpha variant S, which harbors a P681H mutation and the D614G S (Figure 3B). This difference in processing efficiency was not discernible in the lentiviral pseudotype system (Figure 3A). In addition, we tested a previously described deletion mutant (del675-679) (Figure 1A), often generated during cell culture adaptation of SARS-CoV-2. Although the furin

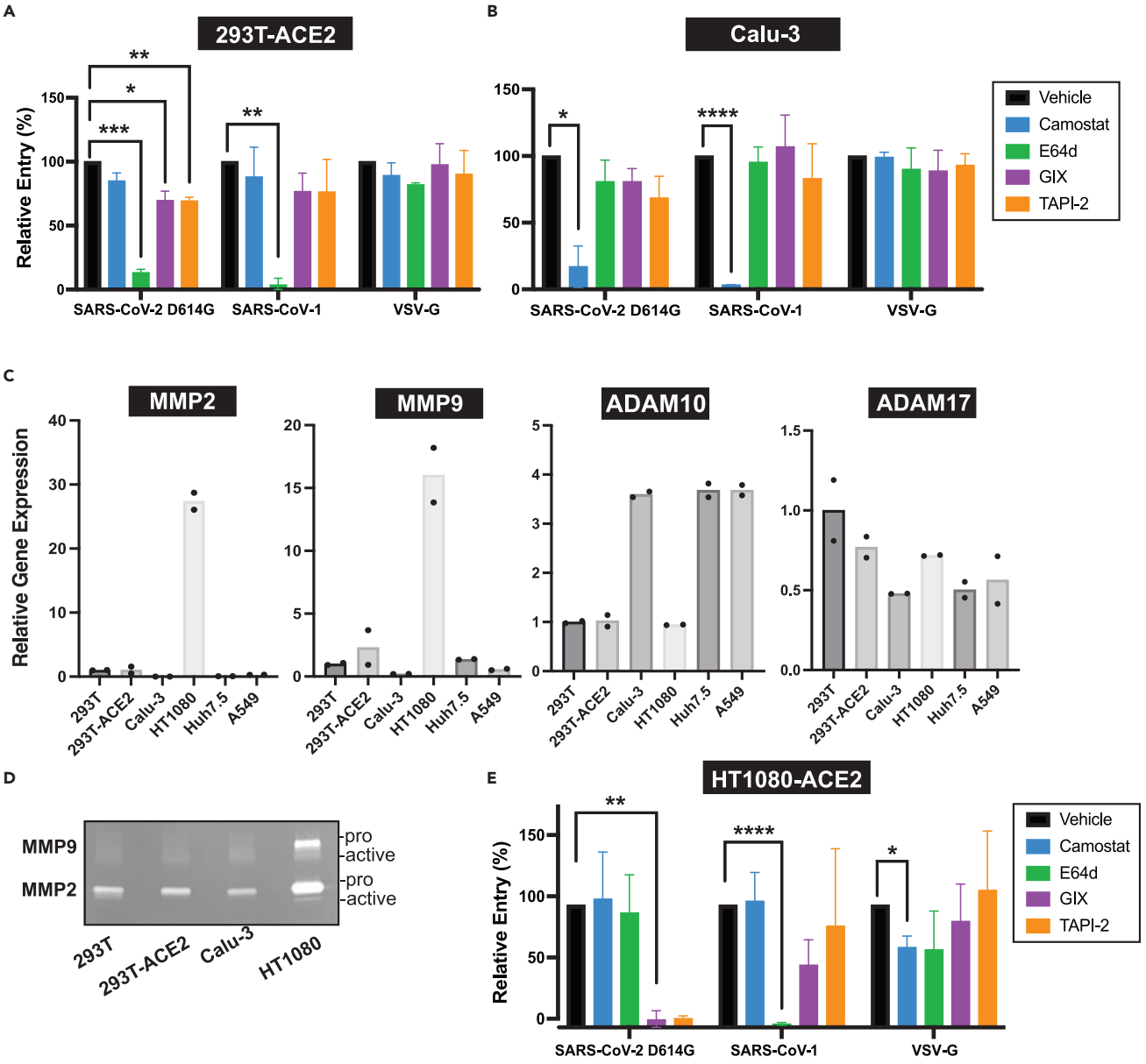

Figure 2. SARS-CoV-2 S can mediate viral entry using a metalloproteinase-dependent entry route in cells expressing high levels of MMP-2 and MMP-9

(A, B, and E) 293T-ACE2, Calu-3, and HT1080 transfected with ACE2, were pre-treated for 1 h with 25 μM Camostat, 10 μM E64days, 40 μM TAPI-2, 10 μM GIX or Vehicle (DMSO) followed by the addition of lentiviral pseudoviruses encoding LacZ and bearing the SARS-CoV-2 D614G S, SARS-CoV-1 S, or VSV-G. After 48 h, cells were fixed and stained with X-gal overnight at 37°C and foci representing infected cells were counted. Relative infection was calculated as the number of foci in the indicated inhibitor treatment relative to vehicle treatment. Each bar graph shows the mean of triplicate values of 3 independent experiments with error bars showing SD. The impact of inhibitors on infection compared to vehicle was analyzed using a two-way ANOVA and Dunnett's post-hoc analysis. P-value lower than 0.05 was used to indicate a statistically significant difference (****, $p < 0.0001$, ***, $p < 0.001$, **, $p < 0.01$, *, $p < 0.05$). (C) Relative mRNA levels of MMP-2, MMP-9, ADAM10, and ADAM17 in various cell lines were measured by RT-qPCR. The level of actin mRNA expression in each sample was used to standardize the data, and normalization on 293T gene expression was performed. (293T, 293T-ACE2, Calu-3, HT1080: $n \geq 3$). (D) Gelatin zymogram of 40 μg of protein from conditioned media (24 h) from indicated cell lines reveals secreted MMP-2 (72 kDa) and MMP-9 (92 kDa) activity, arrows indicate the pro- and active- MMP-2 or MMP-9. Representative image of 3 independent experiments.
See also Figure S2.

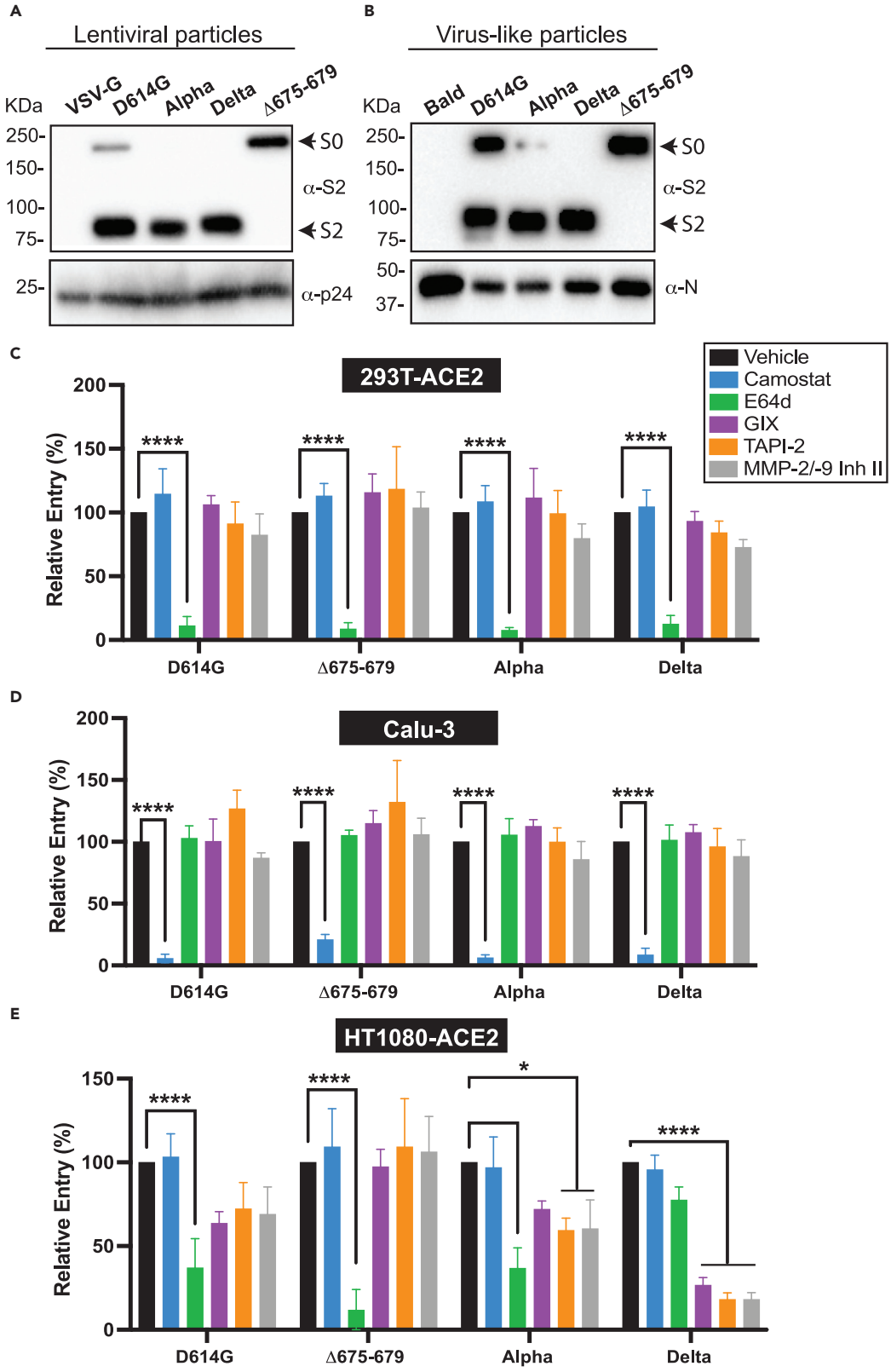
A
Lentiviral particles
KDa
VSV-G
D614G
Alpha
Delta
Δ675-679
250-
150-
100-
75-
25-
S0
α-S2
S2
α-p24
B
Virus-like particles
KDa
Bald
D614G
Alpha
Delta
Δ675-679
250-
150-
100-
75-
50-
37-
S0
α-S2
S2
α-N
C
293T-ACE2
Vehicle
Camostat
E64d
GIX
TAPI-2
MMP-2/-9 Inh II
Relative Entry (%)
200
150
100
50
0
****
D614G
Δ675-679
Alpha
Delta
D
Calu-3
Relative Entry (%)
****
D614G
Δ675-679
Alpha
Delta
E
HT1080-ACE2
Relative Entry (%)
150
100
50
0
****
*
****
D614G
Δ675-679
Alpha
Delta

Figure 3. Delta viral-like particles preferentially use the metalloproteinase-dependent entry pathway in HT1080-ACE2 cells

(A and B) S processing onto purified lentiviral (LVP) and virus-like particles (VLP) was analyzed by immunoblot using an anti-S2 antibody allowing the detection of S0 and S2. As for controls, anti-p24 and anti-N antibodies were used for LVP and VLP respectively. Representative blot of 3 independent experiment is shown.

(C–E) VLP entry assay on 293T-ACE2, Calu-3, and HT1080-ACE2 cells pre-treated for 1 h with 25 μM Camostat, 10 μM E64days, 40 μM TAPI-2, 10 μM GIX, 20 μM MMP-2/9 inhibitor or Vehicle (DMSO). VLP entry was measured 24 h post-infection by measuring the activity of the luciferase reporter. Each bar shows the mean of triplicate values of 3 independent experiments (n = 3) with SD. Significance was determined by ANOVA (one-way ANOVA) followed by a Dunnett's multiple comparisons test. P-value lower than 0.05 was used to indicate a statistically significant difference (****, $p < 0.0001$, ***, $p < 0.001$, **, $p < 0.01$, *, $p < 0.05$).

cleavage site is intact, this deletion abrogates S1/S2 processing (Figure 3A) (Vu et al., 2021; Liu et al., 2020; Zou et al., 2021).

We next tested the entry of SARS-CoV-2 VLPs in 293T-ACE2, Calu-3, and HT1080 cells stably expressing ACE2 (HT1080-ACE2). Similar to the lentiviral pseudotypes, we found that entry of VLPs harboring S with the D614G mutation or del675-679, or those of Alpha and Delta was strongly inhibited by E64days in 293T-ACE2, and by Camostat in Calu-3 cells (Figures 3C and 3D). However, unlike lentiviral particles, D614G and Alpha VLP entry into HT1080-ACE2 were partially sensitive to E64days, GIX and TAPI-2, while Delta entry was dramatically decreased by GIX and TAPI-2 (Figure 3E). This suggests that Delta S preferentially used the metalloproteinase-dependent pathway. In comparison, del675-679 S-mediated VLP entry was only sensitive to E64days in both 293T-ACE2 and HT1080-ACE2 (Figures 3C and 3E). Given the broad specificity of GIX and TAPI-2, we also tested a specific MMP-2/MMP-9 inhibitor, MMP-2/-9 Inhibitor II, which phenocopied the broad-spectrum metalloproteinase inhibitors (Figures 3C, 3D, 3E) suggesting an important role for MMP-2 and MMP-9 in this pathway. Taken together, these results confirm SARS-CoV-2 entry via a metalloproteinase-dependent route that is enabled by S1/S2 processing.

Matrix metalloproteinases-2 and matrix metalloproteinases-9 knockdown reduces serine protease-independent syncytia formation

The SARS-CoV-2 preferential metalloproteinase entry pathway in HT1080 cells, which express high levels of secreted MMP-2/-9 (Figure 2C), in conjunction with the antiviral activity of the MMP-2/MMP-9 inhibitor II (Figure 3E), strongly suggests that MMP-2 and/or MMP-9 play a role in the metalloproteinase-dependent activation of S. To test this, we sought to knockdown expression of MMP-2 and MMP-9 and measure syncytia formation. We first validated the knockdown efficiency of three Dicer substrate interfering RNAs (DsiRNAs) for both MMP-2 and MMP-9 in HT1080-ACE2 cells by qPCR and gelatin zymography. As expected, mRNA levels, expression, and secretion of both MMP-2/9 were efficiently reduced, albeit not completely, when transfected with their respective DsiRNAs (Figures 4A and 4B). We transfected HT1080-ACE2 cells with the two best DsiRNAs specific for MMP-2, MMP-9, both, or a non-targeting negative control DsiRNA, followed by the transfection of plasmids encoding SARS-CoV-2 S and GFP to test metalloproteinase-dependent fusion (Figures 4C and 4D). Even with incomplete knockdown, we observed a significant decrease in the extent of syncytia formation in the MMP-2 and/or MMP-9 knockdown cells (Figures 4C and 4D). Similar results were obtained using the ZIP venus complementation cell-cell fusion assay (Figure 4E) or 293T cells (Figure S3). Of note, we did not observe an additive effect of knockdown of both MMP-2/-9, suggesting that there might be another S-activating metalloproteinase beside MMP-2/MMP-9 (Figures 4C, 4D, 4E, and S3). These results strongly suggest that MMP-2 and MMP-9 are playing roles in the metalloproteinase-dependent SARS-CoV-2 S-mediated fusion.

Metalloproteinase inhibitors block syncytia formation and reduce the replication of SARS-CoV-2 alpha in HT1080-ACE2 cells

We next sought to validate our findings with native replicative SARS-CoV-2. Alpha was used to infect HT1080-ACE2 cells overnight in the presence of Camostat, E64days, TAPI-2, GIX, or vehicle. The next day, cells were fixed and stained for S protein (S) and nucleocapsid protein (N) to visualize infected cells and cell-based ELISA was performed in parallel to quantify N levels and infection. We found that Alpha infection of the HT1080-ACE2 cells was inhibited, albeit incompletely, in the presence of E64days, GIX, and TAPI-2, while Camostat treatment had no effect (Figures 5A, 5B, and S4), indicating that the Alpha infection of HT1080-ACE2 can occur via cathepsins and metalloproteases, but not serine proteases. Interestingly, we also noted that infection led to the formation of large multinucleated cells in vehicle, Camostat and even in the few E64days-treated infected cells (Figures 5A and S4). This suggested that cathepsin inhibition decreases infection, but not S-mediated cell-cell fusion of the few infected cells. Similarly,

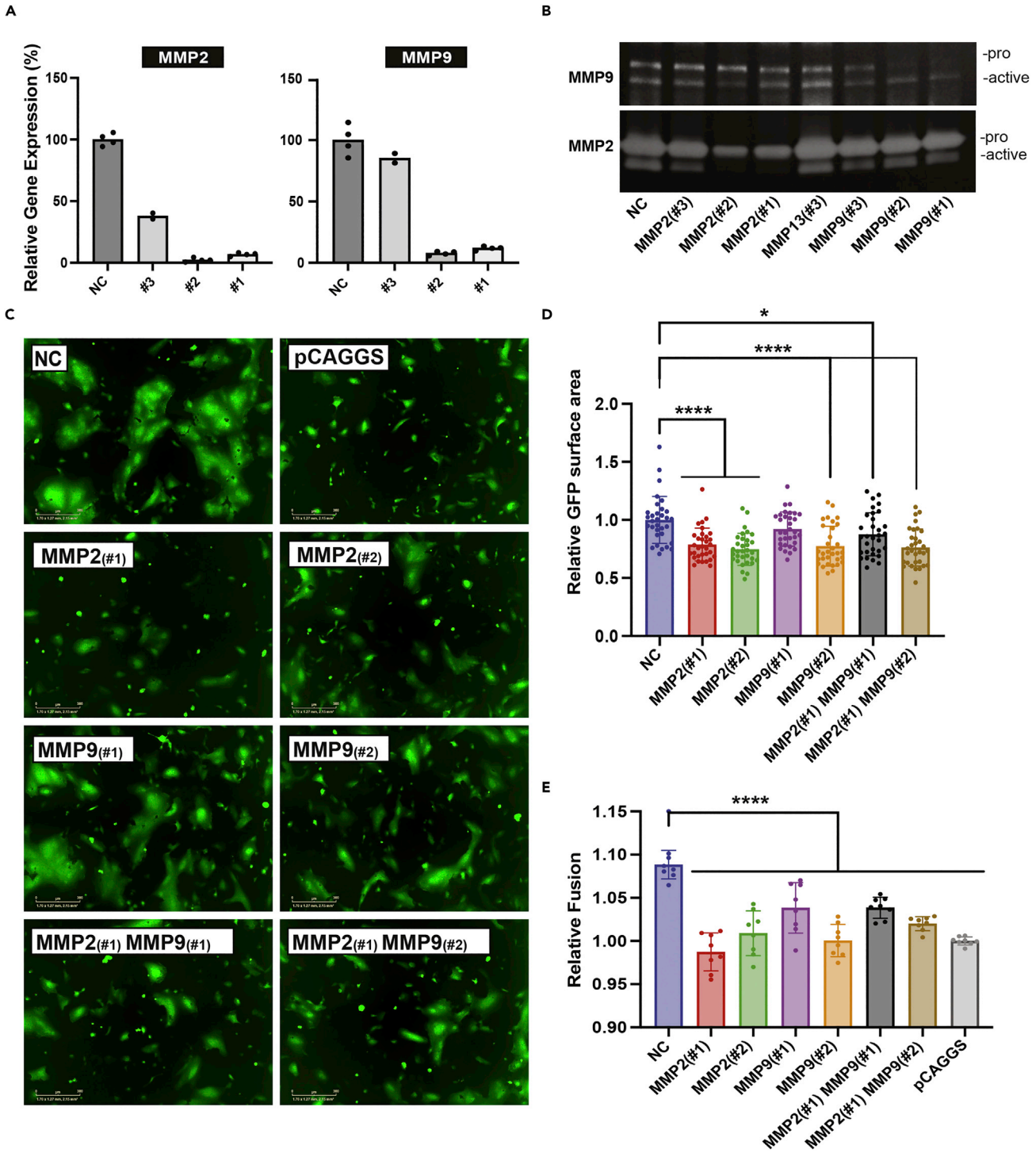

Figure 4. MMP-2/MMP-9 knockdown reduces the metalloproteinase-dependent syncytia formation

(A) HT1080-ACE2 cells were transfected with the indicated DsiRNAs at a final concentration of 10nM, and relative mRNA levels of MMP-2 and MMP-9 were measured by RT-qPCR. The level of actin mRNA expression in each sample was used to standardize the data, and normalization on negative control DsiRNA gene expression was performed.

(B) Gelatin zymogram of 25 μg of protein from conditioned media (24 h) from HT1080-ACE2 cells in (A), arrows indicate the pro- and active- MMP-2 or MMP-9. Representative results of 2 independent experiments are shown.

Figure 4. *Continued*

(C) Representative images of syncytia formation. HT1080-ACE2 cells were transfected with the indicated DsiRNAs alone or in combination (1:1 ratio) at a final concentration of 10 nM for 20 h, followed by transfection with pLV-GFP and D614G spike protein. Images were taken 5 h post-transfection (n = 3). The scale bar represents 300 μm.

(D) Quantification of GFP + surface areas (sixteen images per well) at 5 h post-transfection normalized to non-targeting negative control DsiRNA.

(E) HT1080 (effector) and HT1080-ACE2 (target) cells were transfected with DsiRNAs as described. Effector cells were then transfected with plasmids encoding D614G spike protein and ZipV2 and target HT1080-ACE2 cells were transfected with plasmid encoding ZipV1. A day after transfection, effector and target cells were detached and co-cultured. Bimolecular fluorescence complementation signal was acquired at 5 h of co-culture. Relative fusion is relative to effector cells transfected with pCAGGS instead of the spike protein. Each bar shows the mean of 2-3 independent experiments done in triplicate or quadruplicate with SD. Significance was determined by ANOVA (one-way ANOVA) followed by a Dunnett's multiple comparisons test. p-value lower than 0.05 was used to indicate a statistically significant difference (****, $p < 0.0001$ and *, $p < 0.05$).

See also Figure S3.

metalloproteinase inhibitors also decreased both the number of infected cells and N expression levels (Figures 5A, 5B, and S4). However, unlike E64days, these drugs also completely blocked syncytia formation (Figures 5A and S4), indicating that metalloproteinases facilitate both entry and cell-cell fusion during Alpha infection. Therefore, in agreement with the VLP assays, in HT1080-ACE2 cells, a proportion of Alpha infections proceeded in a cathepsin-dependent manner, while another proceeded in a metalloproteinase-dependent manner.

The Omicron S does not efficiently mediate cell-cell fusion nor use the metalloproteinase-dependent viral entry

Since its emergence and discovery, Omicron has spread rapidly worldwide and became the dominant circulating SARS-CoV-2 variant (Viana et al., 2022). Interestingly, recent studies have reported decreased processing of S and potential reduced activation by TMPRSS2 (Meng et al., 2022; Suzuki et al., 2022). Given that our findings support a model by which metalloproteinase usage is dictated by S cleavage at the S1/S2 junction, we sought to investigate whether the Omicron S could be activated in a metalloproteinase-dependent manner. We first performed cell-cell fusion assays using 293T-ACE2 cells as effector cells in the presence or absence of TMPRSS2 expression (Figure 6A). Interestingly, we found that Omicron S mediated only modest fusion in the absence of TMPRSS2, in contrast to the ancestral, D614G, Alpha, or Delta variant S. As expected, Omicron S fusion activity was enhanced in the presence of TMPRSS2, albeit in a slightly lower extent compared to the other SARS-CoV-2 S tested (Figure 6A). In addition, as previously reported and in accordance with our model, the ratio of S2/S0 in cell lysates was reduced for Omicron when compared to D614G (Figure 6B).

We next assessed the preferential entry route employed by Omicron S using VLPs. We found that similarly to other SARS-CoV-2 variants, Omicron used the endosomal cathepsin-dependent pathway in 293T-ACE2 cells and the surface serine protease-dependent pathway in Calu-3 cells (Figure 6C). Usage of the serine protease entry pathway in Calu-3 by Omicron is also supported by recent reports (Peacock et al., 2022; Bojkova et al., 2022). However, while 293T-ACE2 were as susceptible to D614G or Omicron VLPs, Calu-3 was less susceptible to Omicron VLPs when compared to those harboring Alpha, D614G, and Delta S (Figure S5), suggesting that although Omicron VLPs preferred the surface serine protease pathway in Calu-3, this pathway is not as efficiently used as VLPs harboring other variant S. Importantly, unlike the other variants, Omicron did not use the metalloproteinase-dependent pathway in HT1080-ACE2 cells and strictly used the endosomal route (Figure 6C), indicating a shift in protease usage by Omicron.

Given the importance of S processing for metalloproteinase activation of S, we sought to test whether Omicron S reduced usage of this entry pathway was solely due to inefficient S0 cleavage into S1/S2. To test this, we generated an S chimera that contained a D614G S1 with P681R to improve processing and the S2 of Omicron (Figure 7A) and produced VLPs. As expected, analysis of S onto VLPs revealed that the chimera containing S1 with D614G/P618R and S2 of Omicron was processed more efficiently than Omicron S and to a similar level as the D614G/P681 R S (Figure 7B). We next tested entry sensitivity to E64days or metalloprotease inhibitors in HT1080-ACE2. As expected, Omicron entry was almost completely blocked by E64days and insensitive to metalloprotease inhibitors. Interestingly, entry by the S1 D614G/P618R and S2 Omicron chimera was slightly reduced by metalloproteinase inhibitors and less sensitive to E64days (Figure 7C), suggesting that although the cathepsin entry pathway was preferred, the chimera was able to use the metalloproteinase pathway. However, entry by VLPs bearing the D614G/P618 R S was more sensitive to the metalloprotease inhibitors when compared to the S1 D614G/P618R and S2 Omicron chimera

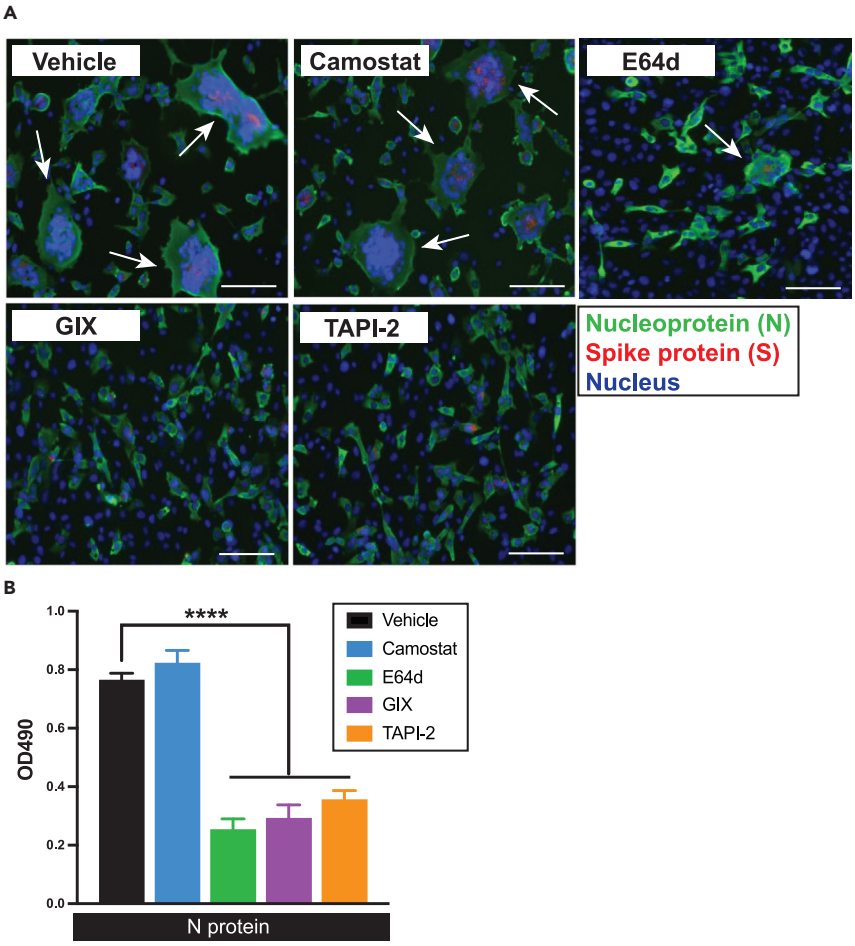

Figure 5. Native Alpha variant infection and the cell fusion of infected cells are blocked by metalloproteinase inhibitors in HT1080-ACE2 cells

(A) Visualization of HT1080-ACE2 syncytia formation after infection by Alpha in presence of indicated inhibitors or vehicle. Cells were treated with Camostat (20 μM), E64days (10 μM), TAPI-2 (20 μM), GIX (10 μM), or Vehicle (DMSO) and then infected with Alpha. After 20 h, cells were washed, blocked, and stained with anti-SARS-CoV-2 spike (S), anti-SARS-CoV-2 nucleocapsid (N) followed by staining with DAPI and fluorescently labeled secondary antibodies. Nuclei, S and N proteins are shown in purple, red, and green respectively. Fluorescent images were acquired with an EVOS™ M7000 Imaging System. Images are representative of 3 independent experiments. Arrows point to syncytia. The scale bar represents 300 μm.

(B) SARS-CoV-2 infection quantification following infection in presence of indicated inhibitors or vehicle. 20 h post-infection, cells were washed, blocked, permeabilized, and stained with mouse anti-SARS-CoV-2 N protein followed by an anti-mouse IgG HRP in conjunction with SIGMAFAST™ OPD developing solution. Optical density (OD) at 490 nm was measured. Each bar shows the mean of triplicate values of 3 independent experiments with error bars showing SD. Significance was determined by ANOVA (one-way ANOVA) followed by a Dunnett's multiple comparisons test. p-value lower than 0.05 was used to indicate a statistically significant difference (****, $p < 0.0001$, ***, $p < 0.001$, **, $p < 0.01$, *, $p < 0.05$).

See also Figure S4.

(Figure 7C). Taken together, although S processing is necessary for metalloproteinase usage, mutations in S2 such as those in Omicron can interfere with the viral entry pathway preference.

DISCUSSION

Previous studies have shown that SARS-CoV-1 and SARS-CoV-2 can enter cells via two distinct ACE2-dependent pathways: a surface serine protease pathway and an endosomal cathepsin protease pathway (Hoffmann et al., 2020b; Shang et al., 2020). Here we show that the SARS-CoV-2 wild-type and variant of concerns (VOCs) S glycoprotein can also be triggered via metalloproteinases, specifically MMP-2 and

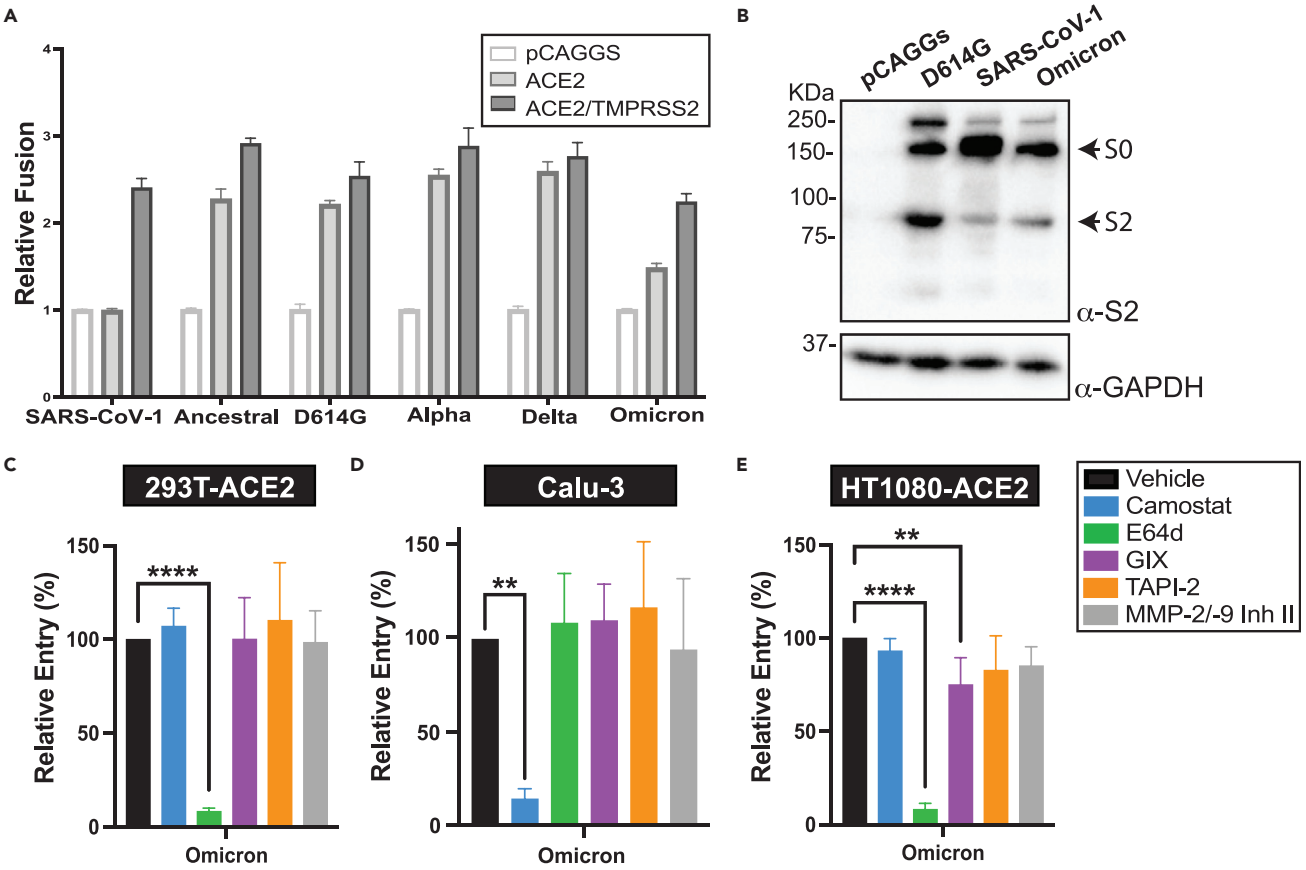

Figure 6. Omicron S is not effectively triggered in a metalloproteinase-dependent manner

(A) Effector 293T cells transfected with plasmids encoding the indicated S, and ZipVenus1, were co-cultured with target 293T cells transfected with plasmids encoding ZipVenus 2, ACE2, and TMPRSS2 or empty vector. Fluorescence generated by the reconstitution of ZIPVenus upon cell-cell fusion was measured at 4 h of co-culture (1:1 ratio). Bar graph shows the mean of quadruplicate values of a representative experiment of 3 independent experiments with error bars showing SD.

(B) S processing in effector 293T cells was analyzed by immunoblot using an anti-S2 antibody allowing the detection of S0 and S2. As for loading control, anti-GAPDH antibody was used. Representative image of 3 independent experiments.

(C–E) Omicron Spike VLP entry assay on (C) 293T-ACE2, (D) Calu-3, and (E) HT1080-ACE2 cells pre-treated for 1 h with 25 μM Camostat, 10 μM E64days, 40 μM TAPI-2, 10 μM GIX, 20 μM MMP-2/9 Inhibitor or Vehicle (DMSO). VLP entry was measured 24 h post-infection by measuring the activity of the luciferase reporter. Each bar shows the mean of triplicate values of ≥3 independent experiments with error bars showing SD. Significance was determined by ANOVA (one-way ANOVA) followed by a Dunnett's multiple comparisons test. p-value lower than 0.05 was used to indicate a statistically significant difference (****, $p < 0.0001$, ***, $p < 0.001$, **, $p < 0.01$, *, $p < 0.05$).

See also Figure S5.

MMP-9, for viral entry (Figure 8) and cell-cell fusion. The ability to use this entry pathway required high expression of these proteases and proteolytic processing at the S1/S2 boundary in viral producer cells. Accordingly, usage of this pathway by SARS-CoV-2 variants correlated with differential extents of S processing in viral producer cells; the efficiently processed S of Delta preferentially entered via the metalloproteinase route when available, while S of Omicron was mostly unprocessed and could not be activated via the metalloproteinase pathway. Given that metalloproteinases such as MMP-2/9 are released and highly expressed in the context of lung damage and inflammation during severe COVID-19, this mechanism of activation could play critical roles in S-mediated cytopathic effects, tropism, and overall pathogenesis.

With previous work reporting the presence of syncytia in the lung of deceased patients with COVID-19 (Ou et al., 2020; Bussani et al., 2020), the ability of SARS-CoV-2 S to mediate cell-to-cell fusion has been hypothesized to play roles in both pathogenesis and virus cell-to-cell propagation (Bussani et al., 2020; Zhang et al., 2021; Zeng et al., 2022). The formation of such multinucleated cells is believed to occur by the activation of SARS-CoV-2 S expressed at the cell surface of infected cells (Ding et al., 2021) and fusion with

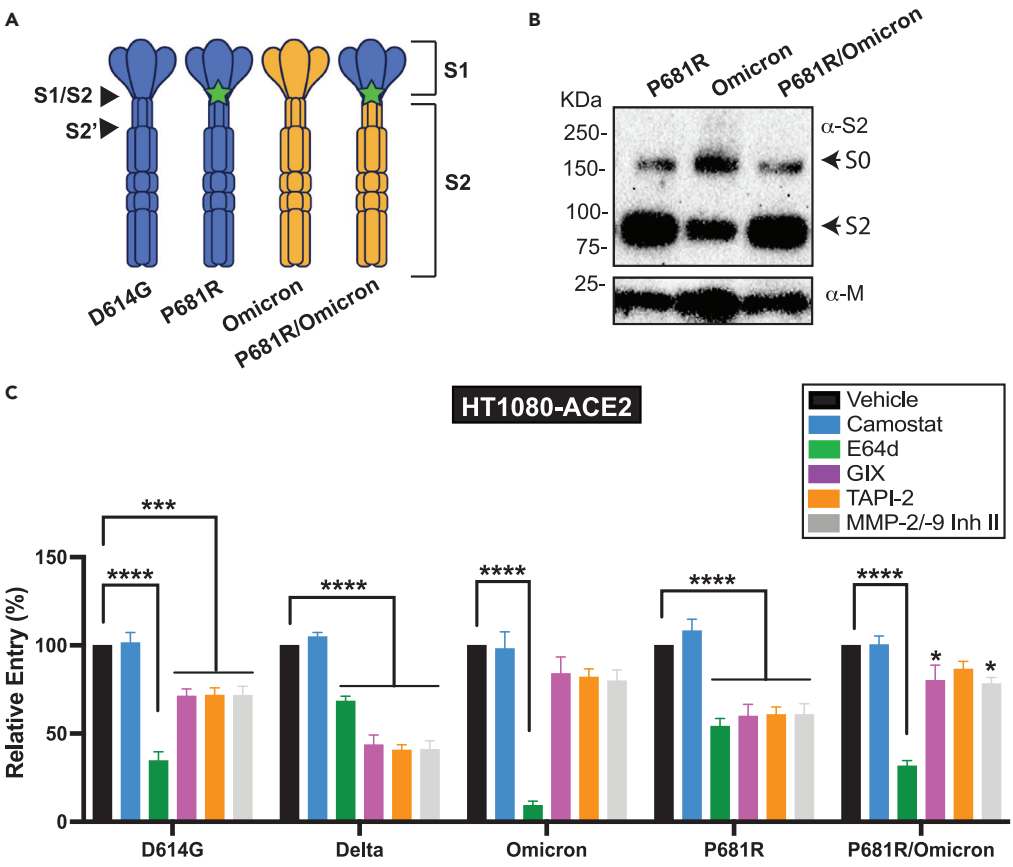

Figure 7. Omicron S chimera with P681R allows MMP-dependent entry

(A and B) (A) Schematics of chimeric S glycoprotein (B) Processing of chimeric S glycoprotein of virus-like particles (VLP) was analyzed by immunoblot using an anti-S2 antibody allowing the detection of S0 and S2. As for control, anti-M antibody was used.

(C) VLP entry assay on HT1080-ACE2 cell pre-treated for 1 h with 25 μM Camostat, 10 μM E64days, 40 μM TAPI-2, 10 μM GIX, 20 μM MMP-2/9 inhibitor or Vehicle (DMSO). VLP entry was measured 24 h post-infection by measuring the activity of the luciferase reporter. Each bar shows the mean of triplicate values of at least 3 independent experiments ($n \geq 3$) with SD. Significance was determined by ANOVA (one-way ANOVA) followed by a Dunnett's multiple comparisons test. p-value lower than 0.05 was used to indicate a statistically significant difference (****, $p < 0.0001$, ***, $p < 0.001$, **, $p < 0.01$, *, $p < 0.05$).

neighboring cells expressing ACE2 and surface serine proteases such as TMPRSS2. However, the relatively low abundance of ACE2+ and TMPRSS2+ cells in the lower airways suggests that there may be additional factors able to activate S (Hou et al., 2020; Hikmet et al., 2020; Zou et al., 2020; Saheb Sharif-Askari et al., 2020). TMPRSS2-independent SARS-CoV-2 S-mediated cell-cell fusion has been previously observed *in vitro* and reported by other studies (Nguyen et al., 2020; Hörnich et al., 2021). Here we show that metalloproteinases, including MMP-2 and MMP-9, are critical factors in SARS-CoV-2 S serine protease-independent fusion (Figures 1E, 4, and 5). More precisely, the knockdown of MMP-2 and MMP-9 reduced S-mediated syncytia formation in the absence of serine proteases (Figure 4). In addition, Alpha infection and replication in cells expressing high levels of MMP-2 and MMP-9 led to the substantial fusion of infected cells that were abrogated by broad-spectrum MMP inhibitors (Figure 5). Several studies have demonstrated increased levels of MMP-2 and MMP-9 in patients with severe COVID-19, which is associated with disease outcomes (Avila-Mesquita et al., 2021; Gelzo et al., 2022; Ueland et al., 2020; Abers et al., 2021). In addition, infiltrating and activated neutrophils, which are potent sources of released MMP-9, are both associated with severe COVID-19 (Meizlish et al., 2021; Huang et al., 2020; Giamarellos-Bourboulis et al., 2020; Schulte-Schrepping et al., 2020; Ardi et al., 2007). Our studies suggest a model by which inflammation and MMP production during COVID-19 could exacerbate virus-induced cytopathic effects further contributing to disease.

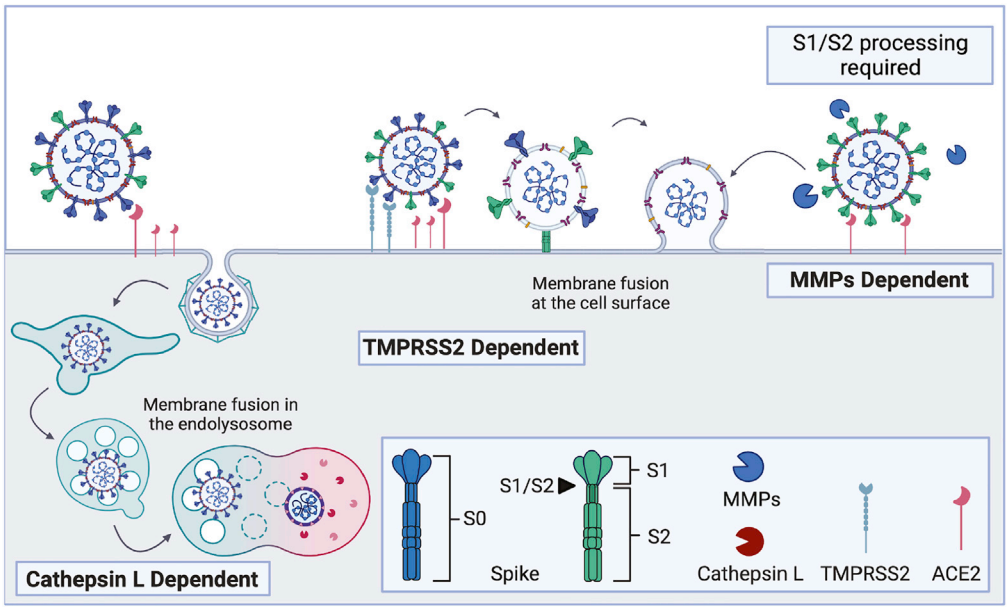

Figure 8. Proposed model of the different SARS-CoV-2 entry pathways

SARS-CoV-2 entry is mediated by the activation of S via proteolytic cleavage by host proteases. In the cathepsin-dependent entry pathway, SARS-CoV-2 is internalized following ACE2 binding and trafficked to endosomes where cathepsin L can cleave and activate unprocessed S (S0) and processed S (S1/S2) for the activation of membrane fusion. In the TMPRSS2-dependent entry pathway, S0 and S1/S2 are activated by TMPRSS2 (or other surface serine proteases such as TMPRSS13) following ACE2 engagement, leading to membrane fusion at the cell surface. In the MMP-dependent entry pathway, only processed S (S1/S2) is activated via MMPs following ACE2 binding allowing membrane fusion.

In this study, we demonstrated that entry of SARS-CoV-2 lentiviral particles, virus-like particles, and authentic Alpha variant into host cells can occur in a metalloproteinase-dependent manner (Figures 2E, 3E, and 5B). This previously unrecognized entry pathway depended on S1/S2 processing in the viral producer cells (Figures 2, 3, 6, and 8). Therefore, this additional entry route is specific to SARS-CoV-2 and cannot be used by SARS-CoV-1, as SARS-CoV-1 S does not contain the critical S1/S2 furin cleavage site. Whether this additional entry pathway unique to SARS-CoV-2 played a role in its high transmissibility remain to be determined. Multiple variants of SARS-CoV-2 have emerged since the beginning of the COVID-19 pandemic, with each having its own sets of mutations that enhance immune escape and/or transmissibility. Interestingly, variants such as Alpha, Delta, Kappa, and more recently Omicron possess mutations within the S1/S2 furin cleavage site. Notably, Delta S harbors the P681R mutation which improves S1/S2 processing and fitness over that of the ancestral virus and Alpha, which possesses the P681H mutation (Arora et al., 2021; Saito et al., 2021; Mlcochova et al., 2021; Twohig et al., 2022). Other studies, including ours, have shown that Omicron S is less efficiently processed at the S1/S2 junction compared to ancestral S, S with a D614G mutation (Figure 6B), and those of VOCs such as Delta (Du et al., 2022; Wang et al., 2021a). Therefore, as expected, we found that Omicron S mediated reduced metalloproteinase-dependent cell-cell fusion (Figure 6A). In addition, VLPs expressing Omicron S were only slightly sensitive to metalloproteinase-dependent entry. Omicron S has three mutations near the furin cleavage site, H655Y, N679K, and P681H; however, the mechanism by which these or other mutations alter S processing remains to be determined. Interestingly, we also found that an increase in Omicron S processing is not sufficient for efficient usage of the metalloproteinase-dependent entry pathway (Figure 7); suggesting that mutations in Omicron S2 likely affect recognition and/or cleavage by MMPs. In addition, whether the inefficient use of the metalloproteinase pathway for the activation of S to mediate viral entry and cell-cell fusion plays a role in the apparent distinct clinical manifestations and tropism of Omicron is unclear (Wolter et al., 2022; Yuan et al., 2022; Lauring et al., 2022; Meng et al., 2022; Maslo et al., 2022). Nonetheless, our findings of an additional entry pathway suggest a potential for increased tropism in the presence of MMPs during inflammation to cells that do not express serine proteases and could play important roles in dissemination and disease severity.

Yamamoto et al. recently reported a SARS-CoV-2 S-mediated metalloproteinase entry pathway in which ADAM10 was partially involved in different cell lines (Yamamoto et al., 2022). Although we have not directly studied a role for ADAM10 and it is still unknown if ADAM10 can cleave SARS-CoV-2 S, our findings and those of Yamamoto and colleagues highlight the promiscuity of SARS-CoV-2 for host protease activation of S and intensifies the hurdles in the usage of host protease inhibitors for therapeutic purposes. In addition, previous studies on the mouse hepatitis virus (MHV), another betacoronavirus, have reported a metalloproteinase-dependent cell-cell fusion and viral entry mechanisms (Phillips et al., 2017), suggesting that metalloproteinases can activate multiple coronavirus S. Interestingly, unlike S activation mediated via cathepsins or surface serine proteases, the S activation triggered via metalloproteinases required prior S processing at the S1/S2 junction (Figures 1D and 3E) (Yamamoto et al., 2021). Although more work is needed to determine whether MMP-2, MMP-9, and other metalloproteinases directly cleave S, the requirement for a processed S suggest that metalloproteinases can only cleave at the S2′ site. Most MMPs can cleave substrates with $PXXX_{Hy}$ motifs in which the hydrophobic residue is often a leucine, but MMP-2 and MMP-9 can also cleave other groups of substrates (Chen et al., 2002; Kridel et al., 2001). For instance, Kridel et al. show that MMP-9 has a distinct preference for Arg at both P(2) and P(1) which could represent a good match to the PSKR|S sequence of SARS-CoV-2 S2′ site (Chen et al., 2002; Kridel et al., 2001). Further studies are required to characterize the specific roles played by the metalloproteinases and to determine the specific S cleavage site involved in the metalloproteinase-dependent entry pathway.

Previous studies investigating immune signatures of severe COVID-19 unveiled vascular endothelial growth factor A (VEGF-A), a disintegrin and metalloproteinases (ADAMs), and matrix metalloproteinases (MMPs) as potential markers for severe disease progression (Syed et al., 2021b; Hardy and Fernandez-Patron, 2021; Carapito et al., 2022). Our data indicate that increased the secretion of MMPs during severe COVID-19 could exacerbate S-mediated cytopathic effects such as syncytia formation. Furthermore, it could also expand tropism by allowing entry in serine protease deficient cells, and potentially even in ACE2 deficient cells promoted by shed ACE2 induced by ADAM17 activity (Heurich et al., 2014). Therefore, usage of the metalloproteinase pathway by current and future circulating SARS-CoV-2 variants could have profound implications for disease severity, outcome, and potential sequelae following recovery. Targeting MMPs, serine proteases, and cathepsins may be useful to reduce SARS-CoV-2 infection and COVID-19 severity.

Limitations of the study

In this study, we used lentiviral pseudotypes, viral-like particles (VLPs), and native replicative SARS-CoV-2 Alpha virus to investigate the metalloproteinase-dependent entry pathway. Omicron (BA.1) S usage of this pathway was investigated with VLPs; however, validation with native replicative virus was not conducted. In addition, specific small-molecule inhibitors and mRNA knockdown were used to reveal a role for MMP-2 and MMP-9 in the activation of SARS-CoV-2 S during cell-cell fusion and entry; however, more work needs to be done to study direct S cleavage by these proteases and identify the specific cleavage sites within S.

STAR★METHODS

Detailed methods are provided in the online version of this paper and include the following:

- KEY RESOURCES TABLE
- RESOURCE AVAILABILITY
  - Lead contact
  - Materials availability
  - Data and code availability
- EXPERIMENTAL MODEL AND SUBJECT DETAILS
  - Cell lines, inhibitors, and antibodies
- METHOD DETAILS
  - SARS-CoV-2 spike cloning and mutagenesis
  - Soluble ACE2 expression and purification
  - Fusion assays
  - RNA extraction, quantitative reverse transcription PCR, and analysis
  - Gelatin zymography

SUPPLEMENTAL INFORMATION

Supplemental information can be found online at https://doi.org/10.1016/j.isci.2022.105316.

ACKNOWLEDGMENTS

We would like to acknowledge technical support from the uOttawa Flow Cytometry & Virometry Core Facility and the uOttawa Cell Biology and Image Acquisition Core Facility. We thank Juan Corredor and Kuganya Nirmalarajah for their help with depositing the Alpha virus sequence to GISAID. We would also like to acknowledge support from the Western University ImPaKT staff for maintaining the facility needed for this work. This research was funded by a Bhagirath Singh Early Career Award in Infection and Immunity to M.C., a COVID-19 Rapid Research grant from the Canadian Institutes of Health Research (CIHR, OV3 170632), and CIHR stream 1 for SARS-CoV-2 Variant Research to M.C. and P.G. Part of this research was also supported by CIHR operating Pandemic and Health Emergencies Research grant #177958, a CIHR stream 1 and 2 for SARS-CoV-2 Variant Research to A.F. Part of this research was also supported by CIHR Operating Grant: Emerging COVID-19 Research Gaps and Priorities #466984 to S.M. This work was also supported by the Sentinelle COVID Quebec network led by the Laboratoire de Santé Publique du Québec (LSPQ) in collaboration with Fonds de Recherche du Québec - Santé (FRQS) and Genome Canada – Génome Québec, and by the Ministère de la Santé et des Services sociaux (MSSS) and the Ministère de l'Économie et Innovation (MEI). Funding was also provided by an operating grant from CIHR from the Canadian 2019 Novel Coronavirus (COVID-19) Rapid Research Funding Opportunity (FRN440388 to JDD and GAD) and an Infrastructure Grant from CFI for the Imaging Pathogens for Knowledge Translation (ImPaKT) Facility (#36287 to JDD and GAD). M.B. was supported by a uOttawa Centre for Infection, Immunity, and Inflammation (CI3) scholarship. K.F. and R.P.M. were supported by Ontario Graduate Scholarships (OGS). C.M.S. was supported by a graduate scholarship from the Natural Sciences and Engineering Research Council of Canada and an OGS. O.EF. was supported by a Work in Biomedical Research (WiBR) scholarship. M.C. is a Canada Research Chair in Molecular Virology and Antiviral Therapeutics (950-232840) and a recipient of an Ontario Ministry of Research, Innovation and Science Early Researcher Award (ER18-14-09). A.F. is a Canada Research Chair on Retroviral Entry (RCHS0235 950-232424). The funders had no role in study design, data collection, and analysis, decision to publish, or preparation of the article.

AUTHOR CONTRIBUTIONS

GAD, JDD, and MC conceived the study. MB, GL, CF, KF, RPM, AP, AA, CMS, GAD, JDD, and MC designed experimental approaches. MB, GL, CF, KF, RPM, AP, AA, CMS, JP, GBB, RD, YB, OEF, JYL, and MC performed experiments. WLS, SM, AF provided resources. MB, GL, CF, KF, RPM, AP, AA, GAD, JDD, and MC analyzed and interpreted results. PMG, GAD, JDD, and MC supervised the study. MB, GL, and MC wrote the original draft. All authors have read and edited the article.

DECLARATION OF INTERESTS

The authors declare that they have no conflict of interest.

INCLUSION AND DIVERSITY

We support inclusive, diverse, and equitable conduct of research.

Received: April 6, 2022
Revised: August 5, 2022
Accepted: October 5, 2022
Published: November 18, 2022

REFERENCES

Abers, M.S., Delmonte, O.M., Ricotta, E.E., Fintzi, J., Fink, D.L., De Jesus, A.A.A., Zarember, K.A., Alehashemi, S., Oikonomou, V., Desai, J.V., et al. (2021). An immune-based biomarker signature is associated with mortality in COVID-19 patients. JCI Insight *6*, e144455. https://doi.org/10.1172/jci.insight.144455.

Ardi, V.C., Kupriyanova, T.A., Deryugina, E.I., and Quigley, J.P. (2007). Human neutrophils uniquely release TIMP-free MMP-9 to provide a potent catalytic stimulator of angiogenesis. Proc. Natl. Acad. Sci. USA *104*, 20262–20267. https://doi.org/10.1073/pnas.0706438104.

Arora, P., Sidarovich, A., Krüger, N., Kempf, A., Nehlmeier, I., Graichen, L., Moldenhauer, A.-S., Winkler, M.S., Schulz, S., Jäck, H.M., et al. (2021). B.1.617.2 enters and fuses lung cells with increased efficiency and evades antibodies induced by infection and vaccination. Cell Rep. *37*, 109825. https://doi.org/10.1016/j.celrep.2021.109825.

Avila-Mesquita, C.D., Couto, A.E.S., Campos, L.C.B., Vasconcelos, T.F., Michelon-Barbosa, J., Corsi, C.A.C., Mestriner, F., Petroski-Moraes, B.C., Garbellini-Diab, M.J., Couto, D.M.S., et al. (2021). MMP-2 and MMP-9 levels in plasma are altered and associated with mortality in COVID-19 patients. Biomed. Pharmacother. *142*, 112067. https://doi.org/10.1016/j.biopha.2021.112067.

Belouzard, S., Chu, V.C., and Whittaker, G.R. (2009). Activation of the SARS coronavirus spike protein via sequential proteolytic cleavage at two distinct sites. Proc. Natl. Acad. Sci. USA *106*, 5871–5876. https://doi.org/10.1073/pnas.0809524106.

Bertram, S., Glowacka, I., Müller, M.A., Lavender, H., Gnirss, K., Nehlmeier, I., Niemeyer, D., He, Y., Simmons, G., Drosten, C., et al. (2011). Cleavage and activation of the severe acute respiratory syndrome coronavirus spike protein by human airway trypsin-like protease. J. Virol. *85*, 13363–13372. https://doi.org/10.1128/JVI.05300-11.

Bojkova, D., Widera, M., Ciesek, S., Wass, M.N., Michaelis, M., and Cinatl, J. (2022). Reduced interferon antagonism but similar drug sensitivity in Omicron variant compared to Delta variant of SARS-CoV-2 isolates. Cell Res. *32*, 319–321. https://doi.org/10.1038/s41422-022-00619-9.

Braga, L., Ali, H., Secco, I., Chiavacci, E., Neves, G., Goldhill, D., Penn, R., Jimenez-Guardeño, J.M., Ortega-Prieto, A.M., Bussani, R., et al. (2021). Drugs that inhibit TMEM16 proteins block SARS-CoV-2 spike-induced syncytia. Nature *594*, 88–93. https://doi.org/10.1038/s41586-021-03491-6.

Buchrieser, J., Dufloo, J., Hubert, M., Monel, B., Planas, D., Rajah, M.M., Planchais, C., Porrot, F., Guivel-Benhassine, F., Van Der Werf, S., et al. (2020). Syncytia formation by SARS-CoV-2-infected cells. EMBO J. *39*, e106267. https://doi.org/10.15252/embj.2020106267.

Bussani, R., Schneider, E., Zentilin, L., Collesi, C., Ali, H., Braga, L., Volpe, M.C., Colliva, A., Zanconati, F., Berlot, G., et al. (2020). Persistence of viral RNA, pneumocyte syncytia and thrombosis are hallmarks of advanced COVID-19 pathology. EBioMedicine *61*, 103104. https://doi.org/10.1016/j.ebiom.2020.103104.

Carapito, R., Li, R., Helms, J., Carapito, C., Gujja, S., Rolli, V., Guimaraes, R., Malagon-Lopez, J., Spinnhirny, P., Lederle, A., et al. (2022). Identification of driver genes for critical forms of COVID-19 in a deeply phenotyped young patient cohort. Sci. Transl. Med. *14*, eabj7521. https://doi.org/10.1126/scitranslmed.abj7521.

Carter-Timofte, M.E., Arulanandam, R., Kurmasheva, N., Fu, K., Laroche, G., Taha, Z., Van Der Horst, D., Cassin, L., Van Der Sluis, R.M., Palermo, E., et al. (2021). Antiviral potential of the antimicrobial drug atovaquone against SARS-CoV-2 and emerging variants of concern. ACS Infect. Dis. *7*, 3034–3051. https://doi.org/10.1021/acsinfecdis.1c00278.

Chatterjee, D., Tauzin, A., Laumaea, A., Gong, S.Y., Bo, Y., Guilbault, A., Goyette, G., Bourassa, C., Gendron-Lepage, G., Medjahed, H., et al. (2022a). Antigenicity of the Mu (B.1.621) and A.2.5 SARS-CoV-2 spikes. Viruses *14*, 144.

Chatterjee, D., Tauzin, A., Marchitto, L., Gong, S.Y., Boutin, M., Bourassa, C., Beaudoin-Bussières, G., Bo, Y., Ding, S., Laumaea, A., et al. (2022b). SARS-CoV-2 Omicron Spike recognition by plasma from individuals receiving BNT162b2 mRNA vaccination with a 16-weeks interval between doses. Cell Rep. *38*, 110429. https://doi.org/10.1016/j.celrep.2022.110429.

Chen, E.I., Kridel, S.J., Howard, E.W., Li, W., Godzik, A., and Smith, J.W. (2002). A unique substrate recognition profile for matrix metalloproteinase-2. J. Biol. Chem. *277*, 4485–4491. https://doi.org/10.1074/jbc.M109469200.

Ding, S., Adam, D., Beaudoin-Bussières, G., Tauzin, A., Gong, S.Y., Gasser, R., Laumaea, A., Anand, S.P., Privé, A., Bourassa, C., et al. (2021). SARS-CoV-2 spike expression at the surface of infected primary human airway epithelial cells. Viruses *14*, 5.

Du, X., Tang, H., Gao, L., Wu, Z., Meng, F., Yan, R., Qiao, S., An, J., Wang, C., and Qin, F.X.-F. (2022). Omicron adopts a different strategy from Delta and other variants to adapt to host. Signal Transduct. Target. Ther. *7*, 45. https://doi.org/10.1038/s41392-022-00903-5.

Fu, X., Tao, L., and Zhang, X. (2021). Comprehensive and systemic optimization for improving the yield of SARS-CoV-2 spike pseudotyped virus. Mol. Ther. Methods Clin. Dev. *20*, 350–356. https://doi.org/10.1016/j.omtm.2020.12.007.

Gasser, R., Cloutier, M., Prévost, J., Fink, C., Ducas, É., Ding, S., Dussault, N., Landry, P., Tremblay, T., Laforce-Lavoie, A., et al. (2021). Major role of IgM in the neutralizing activity of convalescent plasma against SARS-CoV-2. Cell Rep. *34*, 108790. https://doi.org/10.1016/j.celrep.2021.108790.

Gelzo, M., Cacciapuoti, S., Pinchera, B., De Rosa, A., Cernera, G., Scialò, F., Comegna, M., Mormile, M., Fabbrocini, G., Parrella, R., et al. (2022). Matrix metalloproteinases (MMP) 3 and 9 as biomarkers of severity in COVID-19 patients. Sci. Rep. *12*, 1212. https://doi.org/10.1038/s41598-021-04677-8.

Giamarellos-Bourboulis, E.J., Netea, M.G., Rovina, N., Akinosoglou, K., Antoniadou, A., Antonakos, N., Damoraki, G., Gkavogianni, T., Adami, M.E., Katsaounou, P., et al. (2020). Complex immune dysregulation in COVID-19 patients with severe respiratory failure. Cell Host Microbe *27*, 992–1000.e3. https://doi.org/10.1016/j.chom.2020.04.009.

Glowacka, I., Bertram, S., Müller, M.A., Allen, P., Soilleux, E., Pfefferle, S., Steffen, I., Tsegaye, T.S., He, Y., Gnirss, K., et al. (2011). Evidence that TMPRSS2 activates the severe acute respiratory syndrome coronavirus spike protein for membrane fusion and reduces viral control by the humoral immune response. J. Virol. *85*, 4122–4134. https://doi.org/10.1128/JVI.02232-10.

Gobeil Odai, K., O'Dwyer, C., Steenbergen, R., Shaw, T.A., Renner, T.M., Ghorbani, P., Rezaaifar, M., Han, S., Langlois, M.A., Crawley, A.M., et al. (2020). In vitro Hepatitis C virus infection and hepatic choline metabolism. Viruses *12*, 108. https://doi.org/10.3390/v12010108.

Gong, S.Y., Chatterjee, D., Richard, J., Prévost, J., Tauzin, A., Gasser, R., Bo, Y., Vézina, D., Goyette, G., Gendron-Lepage, G., et al. (2021). Contribution of single mutations to selected SARS-CoV-2 emerging variants spike antigenicity. Virology *563*, 134–145. https://doi.org/10.1016/j.virol.2021.09.001.

Hardy, E., and Fernandez-Patron, C. (2021). Targeting MMP-regulation of inflammation to increase metabolic tolerance to COVID-19 pathologies: a hypothesis. Biomolecules *11*, 390.

Harrison, S.C. (2015). Viral membrane fusion. Virology *479–480*, 498–507. https://doi.org/10.1016/j.virol.2015.03.043.

Heurich, A., Hofmann-Winkler, H., Gierer, S., Liepold, T., Jahn, O., and Pöhlmann, S. (2014). TMPRSS2 and ADAM17 cleave ACE2 differentially and only proteolysis by TMPRSS2 augments entry driven by the severe acute respiratory syndrome coronavirus spike protein. J. Virol. *88*, 1293–1307. https://doi.org/10.1128/JVI.02202-13.

Hikmet, F., Méar, L., Edvinsson, Å., Micke, P., Uhlén, M., and Lindskog, C. (2020). The protein expression profile of ACE2 in human tissues. Mol. Syst. Biol. *16*, e9610. https://doi.org/10.15252/msb.20209610.

Hoffmann, M., Kleine-Weber, H., and Pöhlmann, S. (2020a). A multibasic cleavage site in the spike protein of SARS-CoV-2 is essential for infection of human lung cells. Mol. Cell *78*, 779–784.e5. https://doi.org/10.1016/j.molcel.2020.04.022.

Hoffmann, M., Kleine-Weber, H., Schroeder, S., Krüger, N., Herrler, T., Erichsen, S., Schiergens, T.S., Herrler, G., Wu, N.-H., Nitsche, A., et al. (2020b). SARS-CoV-2 cell entry depends on ACE2 and TMPRSS2 and is blocked by a clinically proven protease inhibitor. Cell *181*, 271–280.e8. https://doi.org/10.1016/j.cell.2020.02.052.

Hoffmann, M., Hofmann-Winkler, H., Smith, J.C., Krüger, N., Arora, P., Sørensen, L.K., Søgaard, O.S., Hasselstrøm, J.B., Winkler, M., Hempel, T., et al. (2021). Camostat mesylate inhibits SARS-CoV-2 activation by TMPRSS2-related proteases and its metabolite GBPA exerts antiviral activity. EBioMedicine *65*, 103255. https://doi.org/10.1016/j.ebiom.2021.103255.

Horby, P., Mafham, B.M., Linsell, L., Bell, J.L., Staplin, N., Emberson, J.R., Wiselka, M., Ustianowski, A., Elmahi, E., Prudon, B., et al.; RECOVERY Collaborative Group (2020). Effect of hydroxychloroquine in hospitalized patients with Covid-19. N. Engl. J. Med. *383*, 2030–2040. https://doi.org/10.1056/NEJMoa2022926.

Hörnich, B.F., Großkopf, A.K., Schlagowski, S., Tenbusch, M., Kleine-Weber, H., Neipel, F., Stahl-Hennig, C., and Hahn, A.S. (2021). SARS-CoV-2 and SARS-CoV spike-mediated cell-cell fusion differ in their requirements for receptor expression and proteolytic activation. J. Virol. *95*, e00002–e00021. https://doi.org/10.1128/JVI.00002-21.

Hou, Y.J., Okuda, K., Edwards, C.E., Martinez, D.R., Asakura, T., Dinnon, K.H., 3rd, Kato, T., Lee, R.E., Yount, B.L., Mascenik, T.M., et al. (2020). SARS-CoV-2 reverse genetics reveals a variable infection gradient in the respiratory tract. Cell *182*, 429–446.e14. https://doi.org/10.1016/j.cell.2020.05.042.

Huang, C., Wang, Y., Li, X., Ren, L., Zhao, J., Hu, Y., Zhang, L., Fan, G., Xu, J., Gu, X., et al. (2020). Clinical features of patients infected with 2019 novel coronavirus in Wuhan, China. Lancet (London, England) *395*, 497–506. https://doi.org/10.1016/S0140-6736(20)30183-5.

Jackson, C.B., Farzan, M., Chen, B., and Choe, H. (2022). Mechanisms of SARS-CoV-2 entry into cells. Nat. Rev. Mol. Cell Biol. *23*, 3–20. https://doi.org/10.1038/s41580-021-00418-x.

Jennewein, M.F., MacCamy, A.J., Akins, N.R., Feng, J., Homad, L.J., Hurlburt, N.K., Seydoux, E., Wan, Y.H., Stuart, A.B., Edara, V.V., et al. (2021). Isolation and characterization of cross-neutralizing coronavirus antibodies from COVID-19+ subjects. Cell Rep. *36*, 109353. https://doi.org/10.1016/j.celrep.2021.109353.

Kishimoto, M., Uemura, K., Sanaki, T., Sato, A., Hall, W.W., Kariwa, H., Orba, Y., Sawa, H., and Sasaki, M. (2021). TMPRSS11D and TMPRSS13 activate the SARS-CoV-2 spike protein. Viruses *13*, 384. https://doi.org/10.3390/v13030384.

Koch, J., Uckeley, Z.M., Doldan, P., Stanifer, M., Boulant, S., and Lozach, P.-Y. (2021). TMPRSS2 expression dictates the entry route used by SARS-CoV-2 to infect host cells. EMBO J. *40*, e107821. https://doi.org/10.15252/embj.2021107821.

Kridel, S.J., Chen, E., Kotra, L.P., Howard, E.W., Mobashery, S., and Smith, J.W. (2001). Substrate hydrolysis by matrix metalloproteinase-9. J. Biol. Chem. *276*, 20572–20578. https://doi.org/10.1074/jbc.M100900200.

Laporte, M., Raeymaekers, V., Van Berwaer, R., Vandeput, J., Marchand-Casas, I., Thibaut, H.J., Van Looveren, D., Martens, K., Hoffmann, M., Maes, P., et al. (2021). The SARS-CoV-2 and other human coronavirus spike proteins are fine-tuned towards temperature and proteases of the human airways. PLoS Pathog. *17*, e1009500. https://doi.org/10.1371/journal.ppat.1009500.

Lauring, A.S., Tenforde, M.W., Chappell, J.D., Gaglani, M., Ginde, A.A., Mcneal, T., Ghamande, S., Douin, D.J., Tablot, H.K., Casey, J.D., et al. (2022). Clinical severity and mRNA vaccine effectiveness for omicron, delta, and alpha SARS-CoV-2 variants in the United States: a prospective observational study. Preprint at medRxiv. https://doi.org/10.1101/2022.02.06.22270558.

Le Coupanec, A., Desforges, M., Kaufer, B., Dubeau, P., Côté, M., and Talbot, P.J. (2021). Potential differences in cleavage of the S protein and type-1 interferon together control human coronavirus infection, propagation, and neuropathology within the central nervous system. J. Virol. *95*. https://doi.org/10.1128/JVI.00140-21.

Letko, M., Marzi, A., Munster, V., and Munster, V. (2020). Functional assessment of cell entry and receptor usage for SARS-CoV-2 and other lineage B betacoronaviruses. Nat. Microbiol. *5*, 562–569. https://doi.org/10.1038/s41564-020-0688-y.

Li, W., Moore, M.J., Vasilieva, N., Sui, J., Wong, S.K., Berne, M.A., Somasundaran, M., Sullivan, J.L., Luzuriaga, K., Greenough, T.C., et al. (2003). Angiotensin-converting enzyme 2 is a functional receptor for the SARS coronavirus. Nature *426*, 450–454. https://doi.org/10.1038/nature02145.

Liu, Z., Zheng, H., Lin, H., Li, M., Yuan, R., Peng, J., Xiong, Q., Sun, J., Li, B., Wu, J., et al. (2020). Identification of common deletions in the spike protein of severe acute respiratory syndrome coronavirus 2. J. Virol. *94*, e00790–e00820. https://doi.org/10.1128/JVI.00790-20.

Lubinski, B., Fernandes, M.H.V., Frazier, L., Tang, T., Daniel, S., Diel, D.G., Jaimes, J.A., and Whittaker, G.R. (2022). Functional evaluation of the P681H mutation on the proteolytic activation of the SARS-CoV-2 variant B.1.1.7 (Alpha) spike. iScience *25*, 103589. https://doi.org/10.1016/j.isci.2021.103589.

Maslo, C., Friedland, R., Toubkin, M., Laubscher, A., Akaloo, T., and Kama, B. (2022). Characteristics and outcomes of hospitalized patients in South Africa during the COVID-19 omicron wave compared with previous waves. JAMA *327*, 583–584. https://doi.org/10.1001/jama.2021.24868.

Meizlish, M.L., Pine, A.B., Bishai, J.D., Goshua, G., Nadelmann, E.R., Simonov, M., Chang, C.H., Zhang, H., Shallow, M., Bahel, P., et al. (2021). A neutrophil activation signature predicts critical illness and mortality in COVID-19. Blood Adv. *5*, 1164–1177. https://doi.org/10.1182/bloodadvances.2020003568.

Meng, B., Abdullahi, A., Ferreira, I.A.T.M., Goonawardane, N., Saito, A., Kimura, I., Yamasoba, D., Gerber, P.P., Fatihi, S., Rathore, S., et al. (2022). Altered TMPRSS2 usage by SARS-CoV-2 Omicron impacts tropism and fusogenicity. Nature *603*, 706–714. https://doi.org/10.1038/s41586-022-04474-x.

Michnick, S.W., Ear, P.H., Landry, C., Malleshaiah, M.K., and Messier, V. (2010). A toolkit of protein-fragment complementation assays for studying and dissecting large-scale and dynamic protein-protein interactions in living cells. Methods Enzymol. *470*, 335–368. https://doi.org/10.1016/s0076-6879(10)70014-8.

Mlcochova, P., Kemp, S.A., Bassi, J., Papa, G., Meng, B., Ferreira, I.A.T.M., Datir, R., Collier, D.A., Albecka, A., Singh, S., et al. (2021). SARS-CoV-2 B.1.617.2 Delta variant replication and immune evasion. Nature *599*, 114–119. https://doi.org/10.1038/s41586-021-03944-y.

Murgolo, N., Therien, A.G., Howell, B., Klein, D., Koeplinger, K., Lieberman, L.A., Adam, G.C., Flynn, J., Mckenna, P., Swaminathan, G., et al. (2021). SARS-CoV-2 tropism, entry, replication, and propagation: considerations for drug discovery and development. PLoS Pathog. *17*, e1009225. https://doi.org/10.1371/journal.ppat.1009225.

Nguyen, H.T., Zhang, S., Wang, Q., Anang, S., Wang, J., Ding, H., Kappes, J.C., and Sodroski, J. (2020). Spike glycoprotein and host cell determinants of SARS-CoV-2 entry and cytopathic effects. J. Virol. *95*, e02304–e02320. https://doi.org/10.1128/JVI.02304-20.

Ou, X., Liu, Y., Lei, X., Li, P., Mi, D., Ren, L., Guo, L., Guo, R., Chen, T., Hu, J., et al. (2020). Characterization of spike glycoprotein of SARS-CoV-2 on virus entry and its immune cross-reactivity with SARS-CoV. Nat. Commun. *11*, 1620.

Peacock, T.P., Goldhill, D.H., Zhou, J., Baillon, L., Frise, R., Swann, O.C., Kugathasan, R., Penn, R., Brown, J.C., Sanchez-David, R.Y., et al. (2021a). The furin cleavage site in the SARS-CoV-2 spike protein is required for transmission in ferrets. Nat. Microbiol. *6*, 899–909. https://doi.org/10.1038/s41564-021-00908-w.

Peacock, T.P., Sheppard, C.M., Brown, J.C., Goonawardane, N., Zhou, J., Whiteley, M., Consortium, P.V., Silva, D., and Barclay, W.S. (2021b). The SARS-CoV-2 variants associated with infections in India, B.1.617, show enhanced spike cleavage by furin. Preprint at bioRxiv. https://doi.org/10.1101/2021.05.28.446163.

Peacock, T.P., Brown, J.C., Zhou, J., Thakur, N., Sukhova, K., Newman, J., Kugathasan, R., Yan, A.W.C., Furnon, W., De Lorenzo, G., et al. (2022). The altered entry pathway and antigenic distance of the SARS-CoV-2 Omicron variant map to separate domains of spike protein. Preprint at bioRxiv. https://doi.org/10.1101/2021.12.31.474653.

Pfeifer, A., Brandon, E.P., Kootstra, N., Gage, F.H., and Verma, I.M. (2001). Delivery of the Cre recombinase by a self-deleting lentiviral vector: efficient gene targeting in vivo. Proc. Natl. Acad. Sci. USA *98*, 11450–11455. https://doi.org/10.1073/pnas.201415498.

Phillips, J.M., Gallagher, T., and Weiss, S.R. (2017). Neurovirulent murine coronavirus JHM.SD uses cellular zinc metalloproteases for virus entry and cell-cell fusion. J. Virol. *91*. e01564–16. https://doi.org/10.1128/jvi.01564-16.

Plescia, C.B., David, E.A., Patra, D., Sengupta, R., Amiar, S., Su, Y., and Stahelin, R.V. (2021). SARS-CoV-2 viral budding and entry can be modeled using BSL-2 level virus-like particles. J. Biol. Chem. *296*, 100103. https://doi.org/10.1074/jbc.RA120.016148.

Raissi, A.J., Scangarello, F.A., Hulce, K.R., Pontrello, J.K., and Paradis, S. (2014). Enhanced potency of the metalloprotease inhibitor TAPI-2 by multivalent display. Bioorg. Med. Chem. Lett. *24*, 2002–2007. https://doi.org/10.1016/j.bmcl.2014.02.007.

Saccon, E., Chen, X., Mikaeloff, F., Rodriguez, J.E., Szekely, L., Vinhas, B.S., Krishnan, S., Byrareddy, S.N., Frisan, T., Végvári, Á., et al. (2021). Cell-type-resolved quantitative

proteomics map of interferon response against SARS-CoV-2. iScience *24*, 102420. https://doi.org/10.1016/j.isci.2021.102420.

Saheb Sharif-Askari, N., Saheb Sharif-Askari, F., Alabed, M., Temsah, M.H., Al Heialy, S., Hamid, Q., and Halwani, R. (2020). Airways expression of SARS-CoV-2 receptor, ACE2, and TMPRSS2 is lower in children than adults and increases with smoking and COPD. Mol. Ther. Methods Clin. Dev. *18*, 1–6. https://doi.org/10.1016/j.omtm.2020.05.013.

Saito, A., Irie, T., Suzuki, R., Maemura, T., Nasser, H., Uriu, K., Kosugi, Y., Shirakawa, K., Sadamasu, K., Kimura, I., et al.; Genotype to Phenotype Japan G2P-Japan Consortium (2021). Enhanced fusogenicity and pathogenicity of SARS-CoV-2 Delta P681R mutation. Nature *602*, 300–306. https://doi.org/10.1038/s41586-021-04266-9.

Schulte-Schrepping, J., Reusch, N., Paclik, D., Baßler, K., Schlickeiser, S., Zhang, B., Krämer, B., Krammer, T., Brumhard, S., Bonaguro, L., et al.; Deutsche COVID-19 OMICS Initiative DeCOI (2020). Severe COVID-19 is marked by a dysregulated myeloid cell compartment. Cell *182*, 1419–1440.e23. https://doi.org/10.1016/j.cell.2020.08.001.

Shang, J., Wan, Y., Luo, C., Ye, G., Geng, Q., Auerbach, A., and Li, F. (2020). Cell entry mechanisms of SARS-CoV-2. Proc. Natl. Acad. Sci. USA *117*, 11727–11734. https://doi.org/10.1073/pnas.2003138117.

Suzuki, R., Yamasoba, D., Kimura, I., Wang, L., Kishimoto, M., Ito, J., Morioka, Y., Nao, N., Nasser, H., Uriu, K., et al.; Genotype to Phenotype Japan G2P-Japan Consortium (2022). Attenuated fusogenicity and pathogenicity of SARS-CoV-2 Omicron variant. Nature *603*, 700–705. https://doi.org/10.1038/s41586-022-04462-1.

Syed, A.M., Taha, T.Y., Tabata, T., Chen, I.P., Ciling, A., Khalid, M.M., Sreekumar, B., Chen, P.-Y., Hayashi, J.M., Soczek, K.M., et al. (2021a). Rapid assessment of SARS-CoV-2–evolved variants using virus-like particles. Science *374*, 1626–1632. https://doi.org/10.1126/science.abl6184.

Syed, F., Li, W., Relich, R.F., Russell, P.M., Zhang, S., Zimmerman, M.K., and Yu, Q. (2021b). Excessive matrix metalloproteinase-1 and hyperactivation of endothelial cells occurred in COVID-19 patients and were associated with the severity of COVID-19. J. Infect. Dis. *224*, 60–69. https://doi.org/10.1093/infdis/jiab167.

Syed, A.M., Ciling, A., Khalid, M.M., Sreekumar, B., Chen, P.-Y., Kumar, G.R., Silva, I., Milbes, B., Kojima, N., Hess, V., et al. (2022). Omicron mutations enhance infectivity and reduce antibody neutralization of SARS-CoV-2 virus-like particles. Preprint at medRxiv. https://doi.org/10.1101/2021.12.20.21268048.

Tang, T., Jaimes, J.A., Bidon, M.K., Straus, M.R., Daniel, S., and Whittaker, G.R. (2021). Proteolytic activation of SARS-CoV-2 spike at the S1/S2 boundary: potential role of proteases beyond furin. ACS Infect. Dis. *7*, 264–272. https://doi.org/10.1021/acsinfecdis.0c00701.

Tauzin, A., Gong, S.Y., Beaudoin-Bussières, G., Vézina, D., Gasser, R., Nault, L., Marchitto, L., Benlarbi, M., Chatterjee, D., Nayrac, M., et al. (2022). Strong humoral immune responses against SARS-CoV-2 Spike after BNT162b2 mRNA vaccination with a 16-week interval between doses. Cell Host Microbe *30*, 97–109.e5. https://doi.org/10.1016/j.chom.2021.12.004.

Tay, M.Z., Poh, C.M., Rénia, L., Macary, P.A., and Ng, L.F.P. (2020). The trinity of COVID-19: immunity, inflammation and intervention. Nat. Rev. Immunol. *20*, 363–374. https://doi.org/10.1038/s41577-020-0311-8.

Twohig, K.A., Nyberg, T., Zaidi, A., Thelwall, S., Sinnathamby, M.A., Aliabadi, S., Seaman, S.R., Harris, R.J., Hope, R., Lopez-Bernal, J., et al.; COVID-19 Genomics UK COG-UK consortium (2022). Hospital admission and emergency care attendance risk for SARS-CoV-2 delta (B.1.617.2) compared with alpha (B.1.1.7) variants of concern: a cohort study. Lancet Infect. Dis. *22*, 35–42. https://doi.org/10.1016/S1473-3099(21)00475-8.

Ueland, T., Holter, J.C., Holten, A.R., Müller, K.E., Lind, A., Bekken, G.K., Dudman, S., Aukrust, P., Dyrhol-Riise, A.M., and Heggelund, L. (2020). Distinct and early increase in circulating MMP-9 in COVID-19 patients with respiratory failure. J. Infect. *81*, e41–e43. https://doi.org/10.1016/j.jinf.2020.06.061.

Ullah, I., Prévost, J., Ladinsky, M.S., Stone, H., Lu, M., Anand, S.P., Beaudoin-Bussières, G., Symmes, K., Benlarbi, M., Ding, S., et al. (2021). Live imaging of SARS-CoV-2 infection in mice reveals that neutralizing antibodies require Fc function for optimal efficacy. Immunity *54*, 2143–2158.e15. https://doi.org/10.1016/j.immuni.2021.08.015.

Viana, R., Moyo, S., Amoako, D.G., Tegally, H., Scheepers, C., Althaus, C.L., Anyaneji, U.J., Bester, P.A., Boni, M.F., Chand, M., et al. (2022). Rapid epidemic expansion of the SARS-CoV-2 Omicron variant in southern Africa. Nature *603*, 679–686. https://doi.org/10.1038/s41586-022-04411-y.

Vu, M.N., Lokugamage, K.G., Plante, J.A., Scharton, D., Johnson, B.A., Sotcheff, S., Swetnam, D.M., Schindewolf, C., Alvarado, R.E., Crocquet-Valdes, P.A., et al. (2021). QTQTN motif upstream of the furin-cleavage site plays key role in SARS-CoV-2 infection and pathogenesis. Preprint at bioRxiv. https://doi.org/10.1101/2021.12.15.472450.

Wan, Y., Shang, J., Graham, R., Baric, R.S., and Li, F. (2020). Receptor recognition by the novel coronavirus from Wuhan: an analysis based on decade-long structural studies of SARS coronavirus. J. Virol. *94*. e00127–20.

Wang, Q., Anang, S., Iketani, S., Guo, Y., Liu, L., Ho, D.D., and Sodroski, J.G. (2021a). Functional properties of the spike glycoprotein of the emerging SARS-CoV-2 variant B.1.1.529. Preprint at bioRxiv. https://doi.org/10.1101/2021.12.27.474288.

Wang, Q., Nair, M.S., Anang, S., Zhang, S., Nguyen, H., Huang, Y., Liu, L., Ho, D.D., and Sodroski, J.G. (2021b). Functional differences among the spike glycoproteins of multiple emerging severe acute respiratory syndrome coronavirus 2 variants of concern. iScience *24*, 103393.

Wolter, N., Jassat, W., Walaza, S., Welch, R., Moultrie, H., Groome, M., Amoako, D.G., Everatt, J., Bhiman, J.N., Scheepers, C., et al. (2022). Early assessment of the clinical severity of the SARS-CoV-2 omicron variant in South Africa: a data linkage study. Lancet *399*, 437–446. https://doi.org/10.1016/S0140-6736(22)00017-4.

Wrapp, D., Wang, N., Corbett, K.S., Goldsmith, J.A., Hsieh, C.-L., Abiona, O., Graham, B.S., and Mclellan, J.S. (2020). Cryo-EM structure of the 2019-nCoV spike in the prefusion conformation. Science *367*, 1260–1263. https://doi.org/10.1126/science.abb2507.

Yamamoto, M., Gohda, J., Kobayashi, A., Tomita, K., Hirayama, Y., Koshikawa, N., Seiki, M., Semba, K., Akiyama, T., Kawaguchi, Y., and Inoue, J.-I. (2021). Metalloproteinase-dependent and TMPRSS2-independnt cell surface entry pathway of SARS-CoV-2 requires the furin-cleavage site and the S2 domain of spike protein. Preprint at bioRxiv. https://doi.org/10.1101/2021.12.14.472513.

Yamamoto, M., Gohda, J., Kobayashi, A., Tomita, K., Hirayama, Y., Koshikawa, N., Seiki, M., Semba, K., Akiyama, T., Kawaguchi, Y., and Inoue, J.I. (2022). Metalloproteinase-dependent and TMPRSS2-independent cell surface entry pathway of SARS-CoV-2 requires the furin cleavage site and the S2 domain of spike protein. mBio *13*, e0051922.

Yu, S., Zheng, X., Zhou, B., Li, J., Chen, M., Deng, R., Wong, G., Lavillette, D., and Meng, G. (2022). SARS-CoV-2 spike engagement of ACE2 primes S2′ site cleavage and fusion initiation. Proc. Natl. Acad. Sci. USA *119*. e2111199119. https://doi.org/10.1073/pnas.2111199119.

Yuan, S., Ye, Z.-W., Liang, R., Tang, K., Zhang, A.J., Lu, G., Ong, C.P., Poon, V.K.-M., Chan, C.C.-S., Mok, B.W.-Y., et al. (2022). The SARS-CoV-2 Omicron (B.1.1.529) variant exhibits altered pathogenicity, transmissibility, and fitness in the golden Syrian hamster model. Preprint at bioRxiv. https://doi.org/10.1101/2022.01.12.476031.

Zang, R., Gomez Castro, M.F., McCune, B.T., Zeng, Q., Rothlauf, P.W., Sonnek, N.M., Liu, Z., Brulois, K.F., Wang, X., Greenberg, H.B., et al. (2020). TMPRSS2 and TMPRSS4 promote SARS-CoV-2 infection of human small intestinal enterocytes. Sci. Immunol. *5*, eabc3582.

Zeng, C., Evans, J.P., Pearson, R., Qu, P., Zheng, Y.-M., Robinson, R.T., Hall-Stoodley, L., Yount, J., Pannu, S., Mallampalli, R.K., et al. (2020). Neutralizing antibody against SARS-CoV-2 spike in COVID-19 patients, health care workers, and convalescent plasma donors. JCI Insight *5*, e143213.

Zeng, C., Evans, J.P., King, T., Zheng, Y.-M., Oltz, E.M., Whelan, S.P.J., Saif, L.J., Peeples, M.E., and Liu, S.-L. (2022). SARS-CoV-2 spreads through cell-to-cell transmission. Proc. Natl. Acad. Sci. USA *119*. e2111400119. https://doi.org/10.1073/pnas.2111400119.

Zhang, C., Zhang, Y., Zhang, S., Wang, Z., Sun, S., Liu, M., Chen, Y., Dong, N., and Wu, Q. (2020). Intracellular autoactivation of TMPRSS11A, an airway epithelial transmembrane serine protease. J. Biol. Chem. *295*, 12686–12696. https://doi.org/10.1074/jbc.RA120.014525.

Zhang, Z., Zheng, Y., Niu, Z., Zhang, B., Wang, C., Yao, X., Peng, H., Franca, D.N., Wang, Y., Zhu, Y., et al. (2021). SARS-CoV-2 spike protein dictates syncytium-mediated lymphocyte elimination. Cell Death Differ. *28*, 2765–2777. https://doi.org/10.1038/s41418-021-00782-3.

Zhang, S., Go, E.P., Ding, H., Anang, S., Kappes, J.C., Desaire, H., Sodroski, J.G., and Gallagher, T. (2022). Analysis of glycosylation and disulfide bonding of wild-type SARS-CoV-2 spike glycoprotein. J. Virol. *96*. e0162621–21. https://doi.org/10.1128/jvi.01626-21.

Zocchi, M.R., Camodeca, C., Nuti, E., Rossello, A., Venè, R., Tosetti, F., Dapino, I., Costa, D., Musso, A., and Poggi, A. (2016). ADAM10 new selective inhibitors reduce NKG2D ligand release sensitizing Hodgkin lymphoma cells to NKG2D-mediated killing. Oncoimmunology *5*, e1123367. https://doi.org/10.1080/2162402X.2015.1123367.

Zou, X., Chen, K., Zou, J., Han, P., Hao, J., and Han, Z. (2020). Single-cell RNA-seq data analysis on the receptor ACE2 expression reveals the potential risk of different human organs vulnerable to 2019-nCoV infection. Front. Med. *14*, 185–192. https://doi.org/10.1007/s11684-020-0754-0.

Zou, W., Xiong, M., Hao, S., Zhang, E.Y., Baumlin, N., Kim, M.D., Salathe, M., Yan, Z., Qiu, J., and Meng, X.-J. (2021). The SARS-CoV-2 transcriptome and the dynamics of the S gene furin cleavage site in primary human airway epithelia. mBio *12*, e01006–e01021. https://doi.org/10.1128/mBio.01006-21.

STAR★METHODS

KEY RESOURCES TABLE

REAGENT or RESOURCE	SOURCE	IDENTIFIER
Antibodies		
Mouse anti-SARS-CoV-1/SARS-CoV-2 Spike Protein S2 (1A9)	ThermoFisher Scientific	Cat#MA5-35946 RRID: AB_2866558
Mouse anti-SARS-CoV-1/SARS-CoV-2 Nucleocapsid (6H3)	ThermoFisher Scientific	Cat#MA5-35943 RRID: AB_2866555
Rabbit polyclonal Anti-GAPDH	Abcam	Cat#ab9485 RRID: AB_307275
Rabbit polyclonal Anti-HIV-1 p24	MilliporeSigma	Cat#SAB3500946
Polyclonal anti-SARS Membrane protein	Novus biologicals	Cat#NB100-56569 RRID: AB_838837
Mouse anti-N protein antibody (clone 1C7)	Bioss Antibodies	Cat#bsm-41411M RRID: AB_2893114
Rabbit anti-SARS-CoV-2 spike protein (clone 007)	Sino Biological	Cat#40150-R007 RRID: AB_2827979
CV3-25	(Jennewein et al., 2021)	N/A
Mouse anti-human TMPRSS2 antibody	Bio-techne	Cat#MAB107231
Alexa Fluor 647-conjugated goat anti-mouse IgG antibody	ThermoFisher Scientific	Cat#A-21235
Anti-mouse IgG HRP secondary antibody	New England BioLabs	Cat#7076S
Anti-rabbit IgG HRP secondary antibody	New England BioLabs	Cat#7074S
Donkey anti-mouse IgG Alexa Fluor Plus 488	Invitrogen	Cat#A32766
Donkey anti-rabbit IgG Alexa Fluor Plus 594	Invitrogen	Cat#A32754
Bacterial and virus strains		
SARS-CoV-2 virus-like particles	(Syed et al., 2021a)	N/A
SARS-CoV-2 pseudovirus particles	This paper	N/A
hCoV-19/Canada/ON-SRI-2021-03/2021 (Alpha, B.1.1.7)	Dr. Samira Mubareka	EPI_ISL_14890767
Chemicals, peptides, and recombinant proteins		
Dulbecco's Modified Eagle's medium (DMEM)	Wisent	Cat#319-005-CL
Fetal bovine serum	Sigma	Cat#F2442
Penicillin/Streptomycin - Glutamine	Wisent	Cat#450-202-EL
FreeStyle 293F expression medium	ThermoFisher Scientific	Cat# 12338002
PBS (PBS)	ThermoFischer Scientific	Cat#10010023
Passive Lysis Buffer	Promega	Cat#E1941
Paraformaldehyde 4%	Fisher Scientific	AAJ19943K2
Puromycin dihydrochloride, Ultra Pure Grade	VWR	97064–280
Lipofectamine RNAiMAX	Thermofisher Scientific	Cat#13778075
ExpiFectamine 293 transfection reagent	ThermoFisher Scientific	Cat# A14525
Lipofectamine LTX reagent	Thermofisher Scientific	Cat#15338030
JetPrime transfection reagent	VWR	Cat#CA89129-924
Ni-NTA agarose	Invitrogen	Cat#R90110
Camostat mesylate	Cayman Chemical	Cat#16018
GI 254023X	Cayman Chemical	Cat#28284
Batimastat	Cayman Chemical	Cat#14742
E64days	MilliporeSigma	Cas#324890

(*Continued on next page*)

Continued

REAGENT or RESOURCE	SOURCE	IDENTIFIER
MMP-2/MMP-9 Inhibitor II	MilliporeSigma	Cat#444249
TAPI-2	Tocris	Cat#6013
Dimethyl sulfoxide (DMSO)	Sigma-Aldrich	Cat #D2650-5X5ML
Protease/Phosphatase Inhibitor Cocktail (100X)	New England BioLabs	5872S
X-Gal	VWR	CA97061-646
Formalin solution, neutral buffered, 10%	MilliporeSigma	HT501128-4L
DAPI	Biotechne	Cat. No. 5748
10% Zymogram Plus (Gelatin) protein gel	Invitrogen	ZY00100BOX
Clarity Western ECL Substrate	Bio-RAD	170–5061
Critical commercial assays		
Luciferase Assay System	Promega	Cat#E1500
RNeasy plus Mini kit	Qiagen	Cat # 74136
iScript advanced cDNA kit	Bio-Rad	Cat #1725036
SYBR Green master mix	ThermoFisher Scientific (Life Technologies)	Cat#4309155
Pierce BCA Protein Assay Kit	Bio-Rad	23227
Experimental models: Cell lines		
HEK293T	ATCC	Cat# CRL-3216; RRID: CVCL_0063
HEK293T-ACE2	(Zhang et al., 2020)	N/A
A549	ATCC	Cat# CCL-185 RRID: CVCL_0023
Huh7.5	(Gobeil Odai et al., 2020)	N/A
HT1080	ATCC	Cat# CCL-121 RRID: CVCL_0317
HT1080-ACE2	This paper	N/A
Calu-3	ATCC	Cat# HTB-55 RRID: CVCL_0609
FreeStyle 293F cells	ThermoFisher Scientific	Cat# R79007; RRID: CVCL_D603
Recombinant DNA		
Soluble ACE2 (residues 1–615 of human ACE2)	(Wrapp et al., 2020)	N/A
pLENTI_hACE2_PURO	Dr. Raffaele De Francesco	Addgene #155295
psPAX2	Dr. Didier Trono	Addgene #12260
pMDG	Dr. Inder Verma	Addgene #12108
pCAGGS-SARS-CoV-2-S-D614G	(Gong et al., 2021)	Addgene #185692
pCAGGS-SARS-CoV-2-S-P681R	This paper	N/A
pCAGGS-SARS-CoV-2-S-R815A	This paper	N/A
pCAGGS-SARS-CoV-2-S-Δ Furin site	This paper	N/A
pCAGGS-SARS-CoV-2-S-Δ675-679	This paper	N/A
pCAGGS-SARS-CoV-2-S-Alpha	(Gong et al., 2021)	Addgene #185691
pCAGGS-SARS-CoV-2-S-Delta	(Gong et al., 2021)	Addgene #185593
pCAGGS-SARS-CoV-2-S-Omicron BA.1	(Chatterjee et al., 2022a, 2022b)	Addgene #185452
pCAGGS-SARS-CoV-2-S Chimera S1: D614G, S2: Omicron BA.1	This paper	N/A

(*Continued on next page*)

Continued

REAGENT or RESOURCE	SOURCE	IDENTIFIER
pCAGGS-SARS-CoV-2-S Chimera S1: D614G, P681R, S2: Omicron BA.1	This paper	N/A
pCAGGS-LTR-GFP	James Cunningham, Brigham and Women's hospital, Boston	N/A
pLX307-TMPRSS2	This paper	N/A
BiFC constructs GCN4 leucine zipper-Venus1 (ZipV1)	(Michnick et al., 2010)	N/A
BiFC constructs GCN4 leucine zipper-Venus2 (ZipV2)	(Michnick et al., 2010)	N/A
pCAGGS-SARS-CoV-2 N protein	(Syed et al., 2021a)	N/A
pCAGGS-SARS-CoV-2 M-IRES-E protein	(Syed et al., 2021a)	N/A
pCAGGS-Luc-PS9	(Syed et al., 2021a)	N/A
Software and algorithms		
Flow Jo v10.5.3	Flow Jo	https://www.flowjo.com/
GraphPad Prism v9.0.0	Graphpad	https://www.graphpad.com/
Microsoft Excel v16	Microsoft Office	https://www.microsoft.com/en-ca/microsoft-365/excel
BioRender	BioRender	http://biorender.com/
Image Lab	Bio-Rad	https://www.bio-rad.com/fr-ca/product/image-lab-software?ID=KRE6P5E8Z
LightCycler 480 Software	Roche	https://lifescience.roche.com/en_ca/products/lightcycler14301-480-software-version-15.html
ImageJ	ImageJ	https://imagej.nih.gov
Imager Software	Agilent	https://www.agilent.com/en/product/cell-analysis/cell-imaging-microscopy/cell-imaging-microscopy-software/biotek-gen5-software-for-imaging-microscopy-1623226
Other		
Biotek Synergy *Neo*2 plate reader	Biotek	N/A
Bio-Rad CFX96™ RT-PCR system	Bio-Rad	N/A
Incucyte-Zoom	EssenBioscience	N/A
Synergy LX multi-mode reader and Gen5 microplate reader	Biotek	N/A
BD LSRFortessa	BD Biosciences	N/A
LightCycler 480 instrument	Roche	N/A

RESOURCE AVAILABILITY

Lead contact

Further information and requests for resources and reagents should be directed to and will be fulfilled by the lead contact, Marceline Côté (Marceline.cote@uottawa.ca).

Materials availability

All materials generated in this study are available upon request. Some of the plasmids generated in this study have been deposited to Addgene (see key resources table).

Data and code availability

Data reported in this paper will be shared by the lead contact upon request. This paper does not report original code. Any additional information required to reanalyze the data reported in this paper is available from the lead contact upon request.

EXPERIMENTAL MODEL AND SUBJECT DETAILS

Cell lines, inhibitors, and antibodies

HEK293T (ATCC), HEK293T-ACE2 (kind gift of Hyeryun Choe, Scripps Research), A549 cells (ATCC), Huh7.5 cells, HT1080 cells (ATCC) and Calu-3 (ATCC) were cultured in Dulbecco's Minimum Essential Medium (DMEM) supplemented with 10% fetal bovine serum (FBS, Sigma), 100 U/mL penicillin, 100 µg/mL streptomycin, and 0.3 mg/mL L-glutamine. HT1080 cells stably expressing ACE2 were generated by infection with lentiviral particles generated with psPAX2, pMDG and pLENTI_hACE2_PURO (gift from Raffaele De Francesco (Addgene plasmid # 155295)) and selection of a polyclonal HT1080-ACE2 cells using 2 µg/mL puromycin. Cells were maintained at 37°C, 5% CO2 and 100% relative humidity.

The inhibitors Camostat mesylate, GI 254023X and Batimastat were purchased from Cayman Chemical. E64days and MMP-2/MMP-9 Inhibitor II were from MilliporeSigma and TAPI-2 from Tocris.

The monoclonal antibodies SARS-CoV-1/SARS-CoV-2 Spike Protein S2 (1A9) and SARS-CoV-1/SARS-CoV-2 Nucleocapsid (6H3) were purchased from ThermoFisher Scientific. The rabbit polyclonal Anti-GAPDH antibody were purchased from Abcam. The rabbit polyclonal Anti-HIV-1 p24 antibody was purchased from MilliporeSigma. The mouse anti-N protein antibody (clone 1C7) was purchased from Bioss Antibodies, and the rabbit anti-SARS-CoV-2 spike protein (clone 007) antibody, was purchased from Sino Biological. Polyclonal SARS Membrane protein antibody was acquired from Novus Biologicals.

METHOD DETAILS

SARS-CoV-2 spike cloning and mutagenesis

The Spike gene sequence from the severe acute respiratory syndrome coronavirus 2 isolate Wuhan-Hu-1 (NC_045512.2) was codon optimized (GeneArt, ThermoFisher) and gene blocks with overlapping sequences were synthesized by Bio Basic Inc (Markham, ON, Canada). The full gene, untagged or with an N-terminal FLAG tag, was reconstituted by Gibson assembly, amplified by PCR, and cloned in pCAGGS. Untagged S mutants (D614G, P681R, R815A, and Δ Furin site (deletion of arginine 682, 683 and 685), Δ675-679, and variants (Alpha, Delta, Omicron BA.1) were generated by overlapping PCR and described elsewhere (Tauzin et al., 2022, Chatterjee et al., 2022a, 2022b; Gong et al., 2021). Chimeras D614G/Omicron and D614G, P681R/Omicron were generated by restriction digestion and ligation of S1/S2 gene fragments.

Soluble ACE2 expression and purification

FreeStyle 293F cells (Invitrogen) were grown in FreeStyle 293F medium (Invitrogen) to a density of 1×10^6 cells/mL at 37°C with 8% CO2 with regular agitation (150 rpm). Cells were transfected with a plasmid coding for His (8) Tagged-ACE2 ectodomain (residues 1–615; (Wrapp et al., 2020)) using ExpiFectamine 293 transfection reagent, as directed by the manufacturer (Invitrogen). One week later, cells were pelleted and discarded. Supernatants were filtered using a 0.22 µm filter (Thermo Fisher Scientific). The soluble ACE2 (sACE2) was purified by nickel affinity columns, as directed by the manufacturer (Invitrogen). The sACE2 preparations were dialyzed against PBS (PBS) and stored in aliquots at −80°C until further use. To assess purity, recombinant proteins were resolved by SDS-PAGE and stained with Coomassie Blue.

Fusion assays

For the syncytium formation assay HEK293T, HEK293T-ACE2, and HT1080-ACE2 cells were seeded in 24-well plates and grown to approximately 80% confluency. Cells were then transiently transfected with plasmid DNA encoding LTR-GFP (kind gift of James Cunningham, Brigham and Women's Hospital, Boston), FLAG-SARS-CoV-2 S WT or indicated mutants, and TMPRSS2 or pCAGGS in a 1:2:5 ratio using jetPRIME (Polyplus-transfection) for HEK293T and HEK293T-ACE2, or lipofectamine LTX plus (Invitrogen) for HT1080-ACE2. Simultaneously, cells were placed in fresh complete media (DMEM supplemented with 10% FBS, 100 U/mL penicillin, 100 µg/mL streptomycin, 0.3 mg/mL L-glutamine) with 25 µM of Camostat or vehicle control DMSO. 24 h post transfection, cells were imaged for syncytium formation using a ZOE Fluorescent Cell Imager (Bio-Rad) and three different fields for each well were obtained.

For the cell-cell fusion assay with soluble ACE2, effector HEK293T cells were transiently transfected with plasmid DNA encoding mCherry, and SARS-CoV-2 S and target HEK293T cells were transiently transfected with plasmid DNA encoding GFP, TMPRSS2 or pCAGGS. 24 h post-transfection, effector and target cells were detached with 0.53 mM EDTA in PBS and co-cultured in complete media at a 1:1 ratio in the presence

of increasing concentrations of soluble ACE2 (0, 25, 50, 100, 150 μg/mL). Cells were imaged 10 h post-co-culture using a ZOE Fluorescent Cell Imager (Bio-Rad).

For the ZipVenus complementation cell fusion assay, HEK293T, HT1080, or HT1080-ACE2 cells were seeded in a 12-well microplate in complete media to achieve 70% confluency the next day. Transient transfections were performed using JetPRIME (Polyplus transfection, France) for HEK293T cells and lipofectamine LTX plus (Invitrogen) for HT1080/HT1080-ACE2 cells, according to the manufacturer's instructions. Target cells were transfected with ZipV1 (0.5 μg) alone or with hACE2/pcDNA3 (0.05 μg) with or without TMPRSS2/pIX307 (0.45 μg). Effector cells population were transfected with ZipV2 (0.5 μg) and SARS-CoV-2-S (0.125 μg). Total DNA was normalized using the empty pCAGGS vector DNA to 1 μg. Following transfection, cells were incubated at 37°C for 24 h. Then, cells were rinsed with PBS and detached with versene (PBS, 0.53 mM EDTA) and counted. 40,000 cells/well or 20,000 cells/well of both populations of HEK293T or HT1080 cells respectively were co-seeded in complete DMEM without phenol red in a 384-well black plate with optical clear bottom and incubated for 3 h for HEK293T cells and 5 h for HT1080 cells at 37°C, 5% CO2. Bimolecular fluorescence complementation (BiFC) signal was acquired using Biotek Synergy *Neo2* plate reader (BioTek) using monochromator set to excitation/emission of 500 and 542 nm. The original BiFC constructs GCN4 leucine zipper-Venus1 (ZipV1) and GCN4 leucine zipper-Venus2 (ZipV2) were sourced from Stephen W. Michnick (Michnick et al., 2010).

RNA extraction, quantitative reverse transcription PCR, and analysis

Total RNA was extracted using Rneasy Mini Kit (Qiagen, 74104) according to manufacturer's instructions. RNA concentrations were determined using Thermo Scientific™ NanoDrop 2000. cDNA was synthesized using iScript™ Reverse Transcription Supermix (Bio-Rad, 1708840) and qRT-PCR analysis was performed using SYBR Green master mix (Life Technologies) on a Bio-Rad CFX96™ RT-PCR system. Primer sequences are shown in Table S1.

Gelatin zymography

HEK293T, HEK293T-ACE2, Calu-3 and HT1080 cells were analyzed for MMP-2 and MMP-9 activity through zymographic analysis. Cells were plated in a 6-well plate, at 70–80% confluency, media was changed for FBS-free DMEM (conditioned media). Conditioned media were collected after 24 h, centrifuged to remove debris and concentrated 10X using Amicon Ultra-Centrifugal filter units with a 10 kDa cutoff (MilliporeSigma). Total protein concentration was measured using the BCA assay (Thermo Scientific). 40 μg of protein per sample were diluted in a non-reducing sample buffer (4% SDS, 20% glycerol, 0.01% bromophenol blue, 125 mM Tris-HCl, pH 6.8) and loaded to a 10% Zymogram Plus (Gelatin) protein gel from Invitrogen. Following electrophoresis, gels were washed twice for 30 min in washing buffer (2.5% Triton X-100, 50 mM Tris-HCl, pH 7.5, 5 mM $CaCl_2$ and 1 μM $ZnCl_2$) at room temperature with gentle agitation. Gels were next incubated overnight at 37° in development buffer (1% Triton X-100, 50 mM Tris-HCl, pH 7.5, 5 mM $CaCl_2$ and 1 μM $ZnCl_2$) to initiate enzymatic activity. Gels were stained with Coomassie Blue 0.5% for 1 h and distained with 10% acetic acid and 40% methanol before being scanned.

TMPRSS2 cell surface staining and flow cytometry analysis

Cells were detached with PBS-EDTA (0.53mM) and washed with PBS to remove excess EDTA. Cells were incubated with PBS (mock) or mouse anti-hTMPRSS2 antibody (Bio-techne, #MAB107231, 5 μg/mL) for 1 h at 4°C. After washing the cells, Alexa Fluor 647-conjugated goat anti-mouse IgG antibody (ThermoFisher, #A-21235, 1:500 dilution) was used as a detection antibody for 20 min at room temperature. After washing, cells were fixed in PBS containing 2% formaldehyde and then acquired on a LSRFortessa (BD Biosciences). Data analysis was performed using FlowJo v.10.5.3 (Tree Star).

Lentiviral pseudotype production and entry assays

HEK293T cells were transiently co-transfected with lentiviral packaging plasmid psPAX2 (gift from Didier Trono, Addgene #12260), lentiviral vector encoding LacZ (LV-LacZ, gift from Inder Verma (Addgene #12108) (Pfeifer et al., 2001), and a plasmid encoding the different S or VSV-G at a 1:1:1 ratio using jetPRIME transfection reagent. The supernatant was harvested at 48, 72, and 96 h post-transfection and filtered with a 0.45 μM filter. Lentivirus particles were concentrated via ultra-centrifugation (20,000 RPM, 1.5 h, 4°C) with a sucrose cushion (20% w/v). Viral particles were resuspended with PBS and stored at −80°C.

Cells were seeded in 96-well plates to achieve approximately 50% confluence after 24 h. After 24 h, cells were pre-incubated with the inhibitor(s) for 1 h diluted in the respective standard growth media with 5 μg/mL polybrene. Concentrated lentiviruses were also diluted in growth media containing polybrene to achieve between 100 and 200 foci following infection. After 24 h incubation with virus and inhibitors, cells were placed in fresh growth media. 72 h post-infection, cells were fixed in formalin and stained with 100 μM X-Gal in staining solution (5 mM potassium ferrocyanide, 2 mM magnesium chloride in PBS) and incubated at 37°C for 16–24 h. Positive foci were manually counted using a light microscope. Inhibitor focus-forming units (FFUs) were normalized to vehicle control.

Viral-like particle production and entry assays

SARS-CoV-2 virus-like particles (VLPs) were produced in HEK293T cells by co-transfection of CoV-2-N (1), CoV-2-*M*-IRES-E (0.5), CoV-2-Spike (0.0125) and Luc-PS9 (1) (Syed et al., 2021a) at indicated ratios using jetPRIME transfection reagent (CoV-2-N, CoV-2-*M*-IRES-E and Luc-PS9 were gifts from Abdullah M. Syed and Jennifer A. Doudna, Gladstone Institute of Data Science and Biotechnology). N protein harboring the R203M substitution was used to enhance assembly and production of VLPs, as previously described (Syed et al., 2022). For the Bald control, the empty vector plasmid, pCAGGS, was transfected instead of the CoV-2-S at similar ratio. Media was changed 24 h post-transfection and supernatants were collected at 48, 72, and 96 h post-transfection and filtered with a 0.45 μM filter. VLPs in supernatants were concentrated as described above for the lentivirus particles.

For VLP infection, cells were seeded in 96-well plates to achieve approximately 70% confluence the following day. After 24 h, cells were pre-incubated with the inhibitor(s) for 1 h diluted in 2% serum growth media with 5 μg/mL polybrene. Concentrated VLPs were also diluted in 2% serum growth media containing polybrene. After 20–24 h incubation with VLP and inhibitors, supernatant was removed, and cells were rinsed in 1X PBS and lysed by the addition of 40 μL passive lysis buffer (Promega) followed by one freeze-thaw cycle. A Synergy *Neo*2 Multi-Mode plate reader (BioTek) was used to measure the luciferase activity of each well after the addition of 50–100 μL of reconstituted luciferase assay buffer (Promega). Inhibitors were normalized to vehicle control.

Knockdown of MMP-2 and MMP-9

HT1080-ACE2 and HEK293T-ACE2 cells were seeded in 24-well plates to achieve 70% confluency after 4–6 h and then transfected with Lipofectamine RNAiMAX (Thermofisher) using the indicated DsiRNAs (IDT, Table S2) at a final concentration of 10nM. Combination of DsiRNA was performed using a 1:1 ratio to obtain a final concentration of 10 nM. After 20 h, HT1080-ACE2 and HEK293T-ACE2 were used to perform the syncytia assay as described above, and media from another 24-well plate prepared in parallel was changed to conditioned media for gelatin zymography. 25 μg of protein was used for gelatin zymography of both 293T-ACE2 and HT1080-ACE2 knockdowns. Time-course imaging of the syncytia formation was performed using an Incucyte-Zoom (EssenBioscience), and sixteen images per well were analyzed in ImageJ to measure the percentage of green surface area over background.

Immunoblots

Cells were washed in PBS and then lysed in cold lysis buffer (1% Triton X-100, 0.1% IGEPAL CA-630, 150mM NaCl, 50mM Tris-HCl, pH 7.5) containing protease and phosphatase inhibitors (Cell Signaling). Proteins in cell lysates were resolved by SDS-PAGE and transferred to polyvinylidenedifluoride (PVDF) membranes. Membranes were blocked for 1 h at RT with blocking buffer (5% skim milk powder dissolved in 25mM Tris, pH 7.5, 150mM NaCl, and 0.1% Tween 20 [TBST]). Blots were washed in TBST and proteins were detected using the indicated primary antibodies (1:1000), HRP-conjugated secondary antibodies (1:3000), and visualized using chemiluminescence according to manufacturer protocol (Bio-Rad Clarity ECL substrate).

Microneutralization assay using live SARS-CoV-2 alpha (B.1.1.7) variant

A previously described *in vitro* microneutralization assay (Ullah et al., 2021; Gasser et al., 2021) was performed with modifications and using the SARS-CoV-2 alpha variant (B.1.1.7 lineage). HT1080-ACE2 cells were cultured in DMEM supplemented with penicillin (100 U/mL), streptomycin (100 μg/mL), HEPES, L-Glutamine (0.3 mg/mL), 10% FBS (all from Thermo Fisher Scientific) and puromycin (1 μg/mL, InvivoGen). Twenty-four hours before infection, 2.5×10^4 HT1080 ACE2 cells were seeded per well of

duplicate 96 well plates in puromycin-deficient DMEM and cultured overnight (37°C/5% CO_2) for cell monolayer to adhere. On the day of infection, a deep well plate was used to perform 1:2 serial dilutions for inhibitors listed below in MEM supplemented with penicillin (100 U/mL), streptomycin (100 μg/mL), HEPES, L-Glutamine (0.3 mg/mL), 0.12% sodium bicarbonate, 2% FBS (all from Thermo Fisher Scientific) and 0.24% BSA (EMD Millipore Corporation). The inhibitors Camostat (range: 40–1.25 μM), TAPI-2 (range: 20–0.675 μM), GI 254023X (range: 40–1.25 μM) and E64days (range: 20–1.25 μM) were included in this assay. MEM + 2% FBS containing DMSO at an equivalent concentration to the above inhibitor dilutions served as the vehicle control. All media was aspirated from 96 well plates seeded with HT1080-ACE2 cells and replaced with 100 μL appropriate inhibitor dilution (or vehicle control). Promptly, 2×10^3 TCID50/mL SARS-CoV-2 alpha variant was prepared in a Biosafety Level 3 laboratory (ImPaKT Facility, Western University) and a volume corresponding to 100 TCID50 virus per well was added to wells already containing inhibitor or vehicle diluted in media. An equivalent volume of media void of virus was added to uninfected control wells. All wells were gently mixed and cultured overnight at 37°C, 5% CO_2.

After overnight culture, media was discarded and replaced with 10% formaldehyde for >24 h to cross-link cell monolayers. Wells were washed with PBS, permeabilized for 15 min with PBS + 0.1% Triton X-100 (BDH Laboratory Reagents), washed again in PBS and then blocked for 1 h with PBS + 3% non-fat milk. At this point, one plate was processed for cell-based ELISA as detailed previously (Ullah et al., 2021) to quantify virus infection. Briefly, a mouse anti-SARS-CoV-2 nucleocapsid (N) protein primary antibody and an anti-mouse IgG HRP secondary antibody in conjunction with SIGMAFAST™ OPD developing solution (Millipore Sigma) permitted SARS-CoV-2 infection quantification. The optical density at 490 nm served as the assay readout and was measured using a Synergy LX multi-mode reader and Gen5 microplate reader and imager software (Agilent).

In parallel and after blocking, the second plate was incubated for 1 h with a primary antibody solution formulated in PBS + 1% non-fat milk containing both mouse anti-N protein (1 μg/mL, clone 1C7) and rabbit anti-SARS-CoV-2 spike protein (1:500 dilution, clone 007) antibodies. Extensive washing with PBS ensued, followed by a 45-min incubation with donkey anti-mouse IgG Alexa Fluor Plus 488 (1 μg/mL, Invitrogen), donkey anti-rabbit IgG Alexa Fluor Plus 594 (2 μg/mL, Invitrogen) antibodies and DAPI (1:1000, Millipore Sigma) in PBS + 0.5% BSA consisting of. All wells were then washed three times in PBS, monolayers were covered with minimal PBS and fluorescence images were acquired with an EVOS™ M7000 Imaging System (Invitrogen).

QUANTIFICATION AND STATISTICAL ANALYSIS

Data are expressed as mean ± SD of the mean (SD). Significance was determined by ANOVA (one-way ANOVA) followed by a Dunnett's multiple comparisons test. A p value lower than 0.05 was used to indicate a statistically significant difference ****, $p < 0.0001$, ***, $p < 0.001$, **, $p < 0.01$, *, p *<0.05. Statistical analyses were performed with GraphPad Prism 9.